Miguel João Bolacha Marques

Bachelor of Science in Micro and Nanotechnologies Engineering

New insights into perovskite semiconductors for electronic applications

Dissertation submitted in partial fulfillment of the requirements for the degree of Master of Science in

Micro and Nanotechnologies Engineering

Supervisor: Dr. Elvira Fortunato, Full Professor, Faculdade de Ciências e Tecnologia da Universidade Nova de Lisboa

Co-supervisor: Dr. Jana Santanu, Post-Doctoral Researcher, Faculdade de Ciências e Tecnologia da Universidade Nova de Lisboa

FACULDADE DE CIÊNCIAS E TECNOLOGIA
UNIVERSIDADE NOVA DE LISBOA

September, 2019

New insights into perovskite semiconductors for electronic applications

If you want it, and it rimes, nature then combines

Acknowledgements

I want to thank Professor Elvira Fortunato for the advises and support given over the last months.

To Doctor Jana Santanu for all the support during laboratory work and thesis doubts.

Aos meus pais e meu irmão, a quem dedico esta dissertação, por toda a paciência e apoio ao longo da minha vida, especialmente durante este último ano. Espero que se divirtam com o meu inglês.

À minha gata Christie, por me ter deixado chateá-la durante os intervalos da escrita.

Para a minha companheira e afilhada Raquel Baltazar, por toda a paciência e carinho demonstrado desde que a conheci, especialmente durante os últimos meses.

Aos meus colegas do CENIMAT Deneb Menda, Raquel Teixeira, Adriana Costa, Emanuel Carlos, Marco Moreira, Renato Nora, Guilherme Ribeiro, Ana Marques, Filipe Sabino, Mariana Matias, Paulo Fernandes e João Rolo, um muito obrigado pelo vosso apoio!

Abstract

Transparent semiconductors are a type of materials distinguished by high transmission of light in visible region and relatively high electrical conductivity. These materials show diverse applications in the fields of solar energy and optoelectronics, being considered one of the most successful everyday products as they're installed everywhere, like window electrodes in smartphones and solar panels.

For n-type semiconductors is easy to obtain high carrier mobility, which is not the case for p-types. Developing p-type high mobility devices proves to be difficult given the nature of valence bands in most oxides, generally leading to large hole effective mass and poor charge conductivity.

This current situation limits advances on thin-films technology, restraining materials band matching possibilities and unfulfilling goal creation of devices with both p- and n-type materials, hence denying improvements in transparent electronics.

However, in recent studies, p-type perovskite-structured semiconductors with low fabrication cost and several applications have shown to possess excellent transparent semiconductor qualities, thus being a potential for the future of electronics and photovoltaics.

In this work, mixed halide – iodine and bromine – organolead-based perovskite semiconductor thin-films ($FAPbBr_xI_{3-x}$) were subjected to absorbance, thickness and structural characterizations, and then, dielectric and conductive layers were added to analyze semiconductor carrier properties, metal-oxide-semiconductor (MOS) capacitance and thin-film transistor (TFT) output.

As a result, p-type and n-type hall mobilities of $20.2cm^2/Vs$ and $38.1cm^2/Vs$, respectively, were achieved by $FAPbBr_xI_{3-x}$ polycrystalline thin-films, negative capacitance and ion migration were identified in MOS capacitors, and relatively high field-effect mobility was estimated for the fabricated TFTs. These analyses show one thing in common, more ambipolar characteristics confirmed by increasing bromine contents.

Keywords: Transparent semiconductors, Organolead mixed-halide perovskites, High-mobility ambipolar thin-films, P-type charge concentration, Polycrystalline ion migration, Negative capacitance

Resumo

Os semicondutores transparentes são um grupo de materiais que se destaca pelas caraterísticas de elevada condutividade elétrica e alta transmitância na região visível da luz, exibindo potencial nos campos da energia solar e optoelectrónica. São considerados dos produtos do dia-a-dia com maior sucesso, uma vez que são instalados em todo o sítio, como em ecrãs, telemóveis e painéis solares.

Para semicondutores do tipo-n, materiais em que os eletrões são os portadores maioritários, é fácil atingir uma elevada mobilidade elétrica, isto é, altos valores de uma grandeza que descreve a facilidade e/ou a tendência para as cargas se movimentarem. O mesmo não se verifica para os materiais do tipo-p, onde as cargas positivas são os portadores maioritários, devido à natureza das bandas de valência na maioria destes materiais. A disposição eletrónica destas estruturas faz com que a massa efetiva das cargas aumente, fenómeno diretamente relacionado com uma diminuição na condutividade elétrica.

Esta situação limita os avanços na tecnologia da eletrónica transparente, não satisfazendo a correspondência entre bandas eletrónicas de vários materiais e, ainda mais importante, negando a possibilidade da fabricação de dispositivos com ambos materiais tipo-n e tipo-p.

No entanto, em estudos recentes, materiais tipo-p com a estrutura perovskite e com baixo custo de produção demonstraram possuir excelentes propriedades de semicondutores transparentes, podendo chegar a constituir parte do futuro da eletrónica.

Neste trabalho, filmes finos de semicondutores de perovskite orgânica-inorgânica baseada em chumbo e na mistura dos halogenetos iodo e bromo ($FAPbBr_xI_{3-x}$), foram sujeitos a análises de absorvância, de espessura e de estruturas cristalinas. De seguida, camadas condutoras e dielétricas foram adicionadas aos filmes finos de forma a analisar a mobilidade elétrica, capacitância (através de um condensador MOS) e corrente (através de um transístor de filme-fino).

Como resultado, mobilidades de hall tipo-p e tipo-n de $20.2cm^2/Vs$ e $38.1cm^2/Vs$, respetivamente, foram obtidas para os filmes-finos policristalinos de $FAPbBr_xI_{3-x}$, perfis de capacitância negativa e migração iónica foram identificados nos condensadores MOS, e relativamente elevada mobilidade de efeito de campo foi estimada para os transístores de filmes-finos fabricados. Os resultados confirmam um acréscimo geral das mobilidades tipo-p e tipo-n e um aumento de caraterísticas ambipolares para semicondutores com maior conteúdo de bromo.

Palavras-chave: Semicondutores transparentes, Perovskite de chumbo baseada em mistura de halogenetos, Filmes finos ambipolares de alta mobilidade, Concentração de cargas do tipo-p, Migração iónica policristalina, Capacitância negativa

Contents

List of Figures

Symbols

ρ	Resistivity (Ω.cm)
t_F	Tolerance factor (a.u.)
μ_F	Octahedral factor (a.u.)
r_A	Effective ionic radius of A cation (10^{-10} m)
r_B	Effective ionic radius of B cation (10^{-10} m)
r_X	Effective ionic radius of X cation (10^{-10} m)
nm	Nanometer (10^{-9} m)
µm	Micrometer (10^{-6} m)
mg	Milligram (10^{-3} kg)
µL	Microliter (10^{-6} L)
M	Molar concentration (mol per liter)
λ	De Broglie wavelength (nm)
Eg	Bandgap energy (electron volts)
x	Bromine molar content (mol)
2θ	X-ray diffraction angle (degrees)
t_C	Carrier lifetime (10^{-9} s)
D_C	Carrier diffusion coefficient (cm^2/s)
V_{GS}	Gate to source voltage (volts)
C_{GS}	Gate to source capacitance (farads)
I_{GS}	Gate to source current (amperes)
V_{DS}	Drain to source voltage (volts)
I_{DS}	Drain to source current (amperes)
${C_{GS}}^{-2}$	Inverse squared capacitance $(farads)^{-2}$
Br	Bromine
I	Iodine
Pb	Lead

Acronyms

TO	Transparent oxide
TCO	Transparent conductive oxide
TOS	Transparent oxide semiconductor
TFT	Thin-film transistor
FA^+	Formamidinium cation
MA^+	Methylammonium cation
MOS	Metal-oxide-semiconductor
LED	Light-emitting diode
CdO	Cadmium Oxide
FPD	Flat-panel display
TCO	Transparent conductive oxide
PCE	Power conversion efficiency
MHP	Metal halide perovskite
MOSFET	Metal-oxide-semiconductor field-effect-transistor
MESFET	Metal-semiconductor field-effect-transistor
MISFET	Metal-insulator-semiconductor field-effect-transistor
PCE	Power conversion efficiency
TF	Thin-film
SSPVD	Single-source physical vapor deposition
PbI_2	Lead iodide
$PbBr_2$	Lead bromide
FAI	Formamidinium iodide
SA	Stearic acid
DMF	Dimethylformamide
NMP	N-methyl-2-pyrrolidone
CH_4N_2O	Urea
$Al(NO_3)_3$	Aluminium nitrate nonahydrate
MET	2-methoxyethanol

ITO	Indium-tin oxide
Al_2O_3	Aluminium oxide
IPA	Isopropyl alcohol
C_6H_5Cl	Anti-solvent chlorobenzene
TGA	Thermogravimetric analysis
SEM	Scanning electron microscope
XRD	X-ray Diffraction
EDX	Energy-dispersive x-ray spectroscopy
FWHM	Full width at half maximum
$FAPbBr_xI_{3-x}$	Formamidinium hybrid perovskite
$MAPbI_3$	Methylammonium iodide perovskite
FET	Field-effect-transistor

Motivation and Objective

Over the last years, perovskite materials have been on top of photovoltaics market. Almost all literature on perovskite involves a definition of a solar cell. What remains unknown is, will there be any other perovskite application scalable to such high point as in photovoltaics?

During laboratory work, it's clear material waste is sometimes present, and the same happens, for instance, to films with a power conversion efficiency still not satisfying for a photovoltaics project. These films could be sent to another group of investigation, allowing different and new characterizations, instead of possibly becoming material wastage.
We are aware that sooner or later all these materials loose their quality with degradation overtime, regardless of their application or destination. Nevertheless, what if it was possible that, those details on freshly made thin-films pointing out for poor photovoltaic performance, could actually be the very same details revealing potential in other devices or applications?

This dissertation work was realized at Universidade Nova de Lisboa in the Department of CENIMAT (Materials Research Center). The aim of this work is to develop semiconductive devices based on organic-inorganic lead-based perovskite thin-films, as they represent one of the most recent progresses in optoelectronics. During lab work, the most important goals were defined as:

1. Building smooth, glassy and low-temperature perovskite thin-films;
2. Achieving high material absorbance, charge-carrier concentration and mobility properties;
3. Building smooth-surfaced thin devices, such as metal-oxide-semiconductor capacitors and thin-film transistors.

1 Introduction

This chapter defines concepts present during development of this work. A brief explanation on materials and devices is made during first sub-chapters and associated deposition techniques const in the final sub-chapter. Theoretical data mentioned will be used for comparison in chapter *Analysis of results*.

1.1 Transparent oxides

Transparent oxides (TOs) are a type of materials distinguished by high transmission of light in visible region and relatively high electrical conductivity. This technology is divided in two groups of materials, transparent conductive oxides (TCOs) and transparent oxide semiconductors (TOSs), allowing applications in the fields of photovoltaics, optoelectronics, biosensing and medicine. TCOs are introduced in electronic circuits to permit high and continuous flow of electric current, whereas TOSs are conductors possessing higher resistivity, with the purpose of controlling the current flow through a certain applied external voltage. Unlike TCOs, TOS devices have the advantage of conducting only when requested. Conductors are older than semiconductors, with cadmium oxide (CdO) powder as the first TCO made in 1902 and indium gallium zinc oxide (IGZO) as the first transparent semiconductor made in 2003 [1-7].

TOs have quite a range of interesting properties. Their potential to reflect thermal infrared heat is driven to make energy-conserving windows and these are the largest area of current use. Front-surface electrodes for solar cells and flat-panel displays (FPDs) benefit from their electrical conductivity and wide bandgaps, electrically controlled smart windows and automatically dimming rear-view mirrors also make use of transparent technology [8].

Over the years, a decrease in resistivity parameter has been necessary as technology becomes more demanding and devices need extra doping properties (fig.1.1). Its reduction involves either an increase in the carrier concentration or in particles mobility, whereas for concentration it will also increase visible absorption, for mobility won't deregulate any other properties. [7, 9-12]

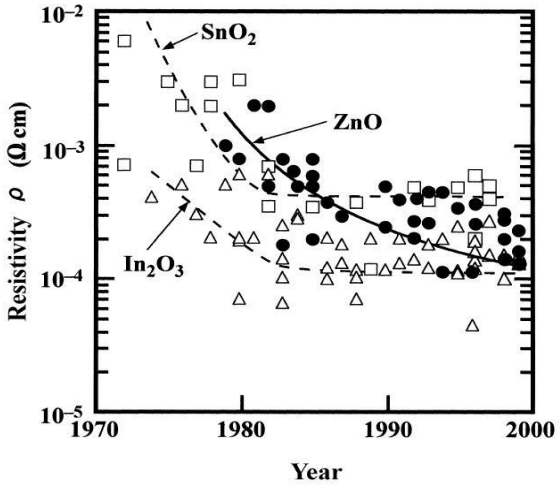

Figure 1.1 - Reported (1970 – 2000) resistivities of TCO materials: SnO2 (square), In2O3 (triangle) and ZnO (circle). [11]

Transparent oxides are mostly commercialized as n-type materials as they reveal higher carrier mobilities, meaning higher conductivity. When comparing electrons to holes while considering the inverse dependence of mobility on effective mass, hole charges possess higher mass values in most occasions, and therefore a higher electrical performance is expected by n-types (fig.1.2). P-types are distinguished by having relatively high resistivity and low carrier concentration, which together with low carrier mobility indicate the presence of self-compensation phenomenon (lattice imperfections such as vacancies) and poor crystalline quality. Developing p-type high mobility proves to be difficult due to the valence band nature in most oxides. Localized electronic orbitals

make these bands very flat leading to large hole effective mass (fig.A1.1 on *Supporting information* appendix) [12-16].
Although p-types situation is limiting advances in TOs technology, recent studies present a group of perovskite-structured materials with low fabrication cost and excellent semiconductor properties that may be a potential for the future of electronics and photovoltaics [15-17].

1.2 Perovskite materials

The name perovskite, which originally referred to a kind of ceramic oxides, is a calcium titanium oxide mineral discovered in 1839. Perovskite became known to the world of Electronics after testing its structure properties and finding several applications in solar cells, photodetectors, light-emitting diodes, transistors and lasing applications. Particularly it captivated serious attention in photovoltaics market due to perovskite high power conversion efficiency (PCE) and low-cost, changing the solar cell efficiency of 3.8% in 2009 to 22.1% in 2017 [18].

With a general molecular formula ABX_3 (A, B being cations and X an anion), perovskite structure follows the geometric Goldschmidt's tolerance factor $t_F = (r_A + r_B)/(\sqrt{2}(r_B + r_X))$ where r_A, r_B and r_X are the effective ionic radius for A, B and X ions, respectively (fig.1.2). Generally, if t_F equals one unit it means it is an ideal cubic structure, which is not always the case as some perovskite structures have a tolerance of $t_F = 0.83$. The farther t_F is from one unit the higher the likelihood for octahedral distortion, influencing future electronic performance [18-20].

For metal halide perovskites (MHPs), molecular formula ABX_3 is more specific. Ion A is usually a monovalent organic cation such as methylammonium ($CH_3NH_3^+$ = MA^+) or formamidinium ($NH_2CH{=}NH_2^+$ = FA^+) and the biggest of the three ions, B is a metal such as lead (Pb+) or tin (Sn+), and X is a halide ion (e.g. I^-, Br^-, Cl^-) with the highest electronegativity of the three ions (fig.A1.2 on *Supporting information* appendix). MHPs demonstrate a fine structure stability in polycrystalline films for $0.81 < t_F < 1.0$ and in single-crystal films for $0.81 < t_F < 1.11$ [21-23].

Although some perovskite inorganic compounds have large bandgaps, none of them have shown potential qualities for *p*-type semiconductors so far. Yet, in recent studies, researchers made use of atomic replacements and first-principles calculations and were able to obtain seven stable layered compounds with sufficiently large bandgaps, optical transparency, light hole effective masses and good p-type conductivities. Therefore, these compounds demonstrate potential to be on the front line of p-type electronics [17].

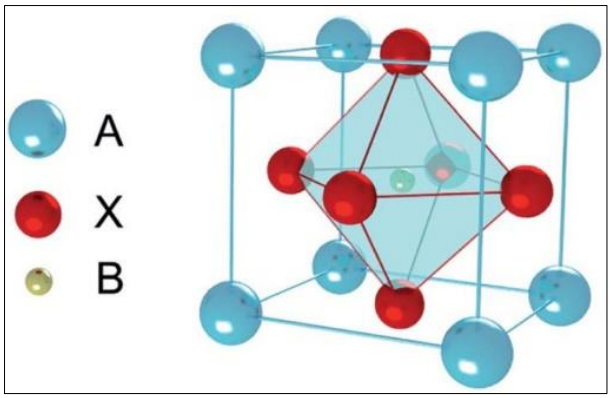

Figure 1.2 - Perovskite structure ABX_3 [18]

Concerning perovskite present researches, organolead hybrid materials – materials with a lead-based, organic-inorganic structure – have shown exceptional optoelectronic properties over the last decade [24]. Lead is the most present B element in the making of perovskite inorganic component (BX_2) due to its stabilizing effect in ABX_3 crystal structures, earth-abundancy and low-cost production [25]. A and X ions such as organic FA^+ and Br^- are added to increase expected numbers of cubic-like structures and ensure thermal stability [26-30]. Other cations such as organic MA^+ or inorganic Cs^+ can stack perovskite in its cubic structure, denying formation of

undesired phases in photovoltaics such as the hexagonal structure, visible during non-perovskite yellow phase [31-34].

Regarding perovskite semiconductors, organic compounds prove to be cheaper and have more flexibility of process-ability, whereas inorganic compounds usually present more thermal stability and higher electrical performance. In order to captivate the best of both worlds, organic-inorganic technology emerged as a promising alternative to silicon, mixing in just one semiconductor properties such as low-temperature synthesis, long carrier lifetime and high absorption coefficient. This is one of the reasons why perovskite is usually produced with one or more organic compounds, such as FA^+ or MA^+ [35-41].

In the light of this fact, researchers naturally start developing new projects based on organic-inorganic perovskites only, such as the introduction of two or more halide ions. Organic–inorganic mixed-halide compounds present higher optical absorption and exhibit better charge transfer characteristics than that of single-halide perovskite. Plus, the diffusion length of electrons and holes in single-halides (such as $MAPbI_3$) is 130 nm (electrons) and 100 nm (holes), whereas for mixed-halides (such as $MAPbI_{3-x}Cl_x$) is 1100 nm (electrons) and 1200 nm (holes), meaning higher diffusion lengths and higher carrier mobilities for the latter compounds. Therefore, mixed-halide perovskites constitute a more ideal absorber layer material for solar cells and several other applications [18].

When a specific compromise of characteristics is required, halide mixing is very important for tolerance factor adjustment, structure stability and high carrier mobility achievement [42]. This perovskite type is obtained by mixing different lead-based precursors (PbX_2), such as lead iodide, lead chloride and lead bromide. For instance, mixing iodine and bromine will form $PbBr_xI_{2-x}$ inorganic precursors that are able to change from hexagonal to orthorhombic structures when increasing bromine contents [43].

According to tolerance factor, studies suggest the formation of cubic structures for $0.9 < t_F \leq 1$, hexagonal structures for $t_F \geq 1$ and tetragonal or orthorhombic structures for $t_F \leq 0.9$. In some cases, achieving cubic crystal structures by a tolerance factor of $0.9 \leq t_F \leq 1$ is not enough, as it also depends on an ionic radius proportion defined by the octahedral factor μ_F. The latter factor is related only to perovskite inorganic components ($\mu_F = r_B/r_X$), where r_B is the lead cationic radius and r_X halide anionic radius. Octahedral factor values confirm optimal cubic structure for $0.414 \leq \mu_F \leq 0.732$ with an average of $\mu_F = 0.573$ [38, 43-50]. Therefore, in addition to mixed-halide configurations, a compromise between tolerance and octahedral factors is also important for achieving desired crystal structures (fig.1.3).

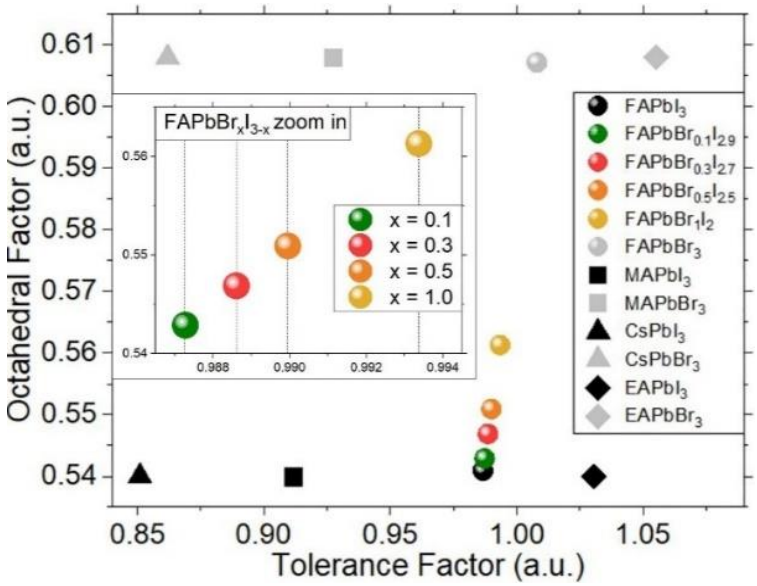

Figure 1.3 - Framing of perovskite examples in a tolerance factor versus octahedral factor mapping [20] with recent effective radius values for the organic cations [32, 47].

1.3 Thin-film transistor

The thin-film transistor (TFT) is a type of field-effect-transistor which is fabricated according to a step-by-step deposition of dielectric, semi-conductive and conductive thin-film layers. It is a device with three terminals (gate, source and drain) and its main purpose is to control the current between source and drain electrodes by varying the potential between gate and source, leading to free charge accumulation at the dielectric/semiconductor interface [51-53].

Thin-film layers are deposited on a substrate (usually non-conductive) according to a specific order, which is similar to the operation principle of the metal-oxide-semiconductor field-effect-transistor (MOSFET). Despite being different in terms of substrate nature and number of terminals, both TFT and MOSFET have the same current purpose and rely on the very same layers interface combination, one being the metal-oxide interface (gate and dielectric layers), and the other being the oxide-semiconductor interface (fig.1.4) [52-56].

The invention of the TFT took place in 1925 and was patented in 1930 by J.E. Lilienfeld and O. Heil. Although there were no practical applications at that time, as thin-film production techniques were yet to be discovered, Lilienfeld describes the important concepts of metal-semiconductor field-effect-transistor (MESFET) and metal-insulator-semiconductor field-effect-transistor (MISFET) in two of his patents. About thirty years later, several devices and semiconductor materials were explored to fabricate TFTs. However, MOSFET silicon-based technology was preferable for the applications at the current date. It was only in the early 1970s that the need for large area applications in flat panel displays motivated the search for alternatives, and TFT technology came along. Nowadays, TFT technology is dominant in the area of displays [51-52, 54-56].

There are several types of TFTs, which can be organized by a list of properties such as device transmittance and insulator's nature. Two important and distinct classes of transistors are the organic TFTs, presenting the advantages of low processing temperature and mechanic flexibility, and the oxide TFTs, devices exhibiting an appealing combination of high optical transparency, high electron mobility and amorphous microstructure. When comparing to other types of technologies, oxide TFTs reveal low manufacturing cost, low leakage current and relatively low process temperature [51-54, 56-57].

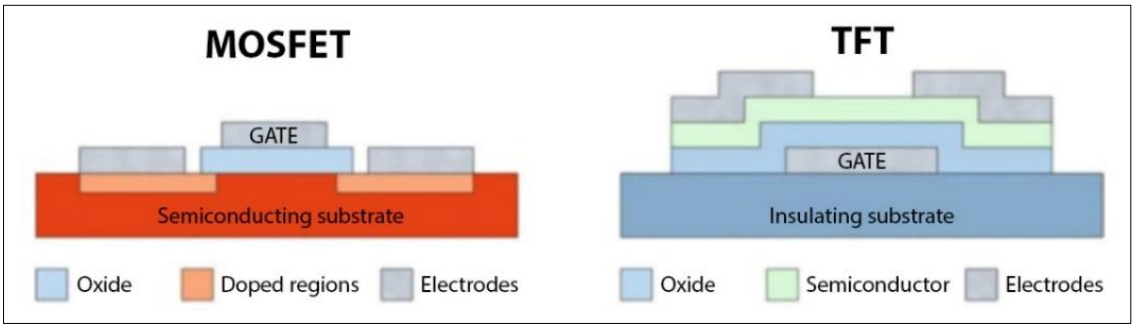

Figure 1.4 - a) Metal-oxide-semiconductor-field-effect-transistor layering structure and b) thin-film-transistor layering structure [52].

1.4 Spin-coating technique

Spin-coating is the oldest and first-based fabrication method used for perovskite TFs fabrication and it can be divided in two most known sub-methods, one-step coating and two-step coating. As perovskite film reveals a slow rate of crystalline growth under room temperature, after spin-coating motion a heat treatment process known as thermal annealing must take place, in order to induce a faster thin-film crystalline growth [58-64].

One-step method produces high crystalline grain-size TFs because crystal growth happens at the same time for all precursors, meaning higher power conversion efficiency (PCE) for perovskite

solar cells (fig.1.5a). However, as organic-inorganic precursors are already mixed and will constitute the same deposited layer, a lack of purity and fine morphology is also verified. Two-step method separates organic from inorganic precursors, promoting a sequential deposition of two layers. As probably expected, films will obtain higher purity with low hybrid reaction rate and a better morphology, but at the same time grain size is also reduced during thermal annealing process (fig.1.5b, c) [61,63-65].

Until the current date, and despite variants like precursors type, dielectric adhesion or room temperature, spin-coating is for all purposes restricted in commercial area by the high percentage of material wastage and necessity for batch processing. In order to obtain perovskite films with better reproducibility and non-toxicity compromises, similar fabrication techniques were tried out shortly after [61,66].

Scientists then developed new methods such as slot-die coating [66-67] and single-source physical vapor deposition (SSPVD) [68], both capable of replacing spin-coating in a near future. Slot-die technique (precision-design ink injection) is considered the most applicable technology to the fabrication of large-area perovskite solar cells, and SSPVD method (powder to gas phase perovskite conversion) is claimed to be worthy of optimization as it provides high purity in a full and uniform thin-film coverage.

However, spin-coating is still the most reported technique and holds the best PCE references, alongside slot-die coating. SSPVD is still in efficiency development, presenting poor photovoltaic properties during the current date. Other methods such as blade-coating and spray-coating are also recent techniques, presenting worse fabrication compromises and less PCE when compared to slot-die coating (fig.1.5d) [61,66-68].

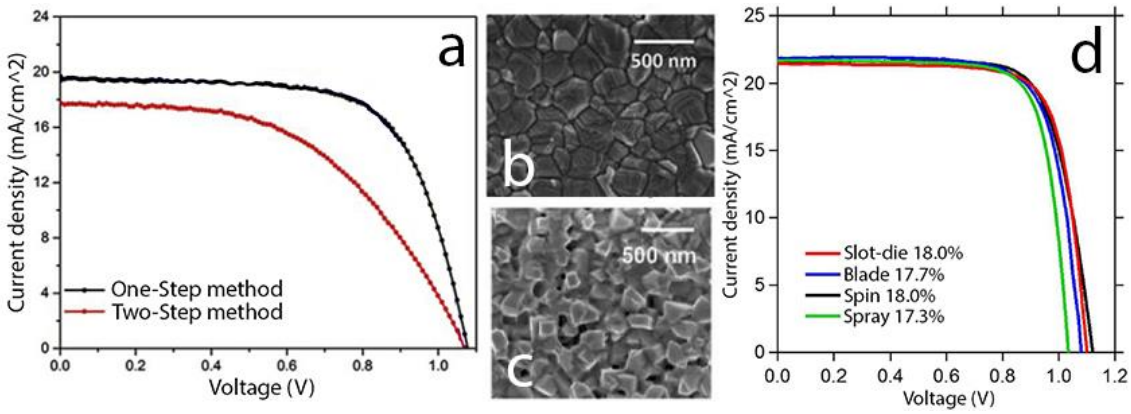

Figure 1.5 – a) Current-voltage curve for measuring perovskite power conversion efficiency (PCE) comparing one-step to two-step spin methods [61]. b), c) one-step and two-step methods film morphology, respectively [61]. d) PCE for several spin-coating based methods [67].

2 Experimental

This chapter regards perovskite materials usage, fabrication processes of all devices and respective characterization methods.

2.1 Materials

Used materials had different distributors. Lead iodide (PbI_2, 99.99%), lead bromide ($PbBr_2$, 98%), formamidinium iodide (FAI, 98%) and stearic acid (SA, 98%) were bought from *Sigma Aldrich*, Dimethylformamide (DMF, 99.9%), N-methyl-2-pyrrolidone (NMP, 99.9%), chlorobenzene (C_6H_5Cl, 99.5%), 2-methoxyethanol (MET, 99%) and urea (CH_4N_2O, 99.5%) were bought from *Fisher Scientific*, aluminium nitrate nonahydrate ($Al(NO_3)_3$, 98%) and indium-tin oxide (ITO) were bought from *Carl Roth* and *Xinyan Technology LTD*, respectively.

2.2 Device Fabrication

Thin-film devices were fabricated according to the following process: Indium tin oxide (ITO) coated glass and silicon substrates with average surface dimensions of 2.5cm x 2.5cm were cleaned by ultrasonication in solutions of soap, deionized water, acetone and isopropyl alcohol, each 10min and sequentially. Substrates then were dried out with nitrogen gun and treated in machine PSD Series for a 30min UV/Ozone irradiation, in order to increase substrates surface energy and wettability. This was the preparation process before each spin-coating deposition, which was made using spin coater model WS-650MZ-23NPP for all deposited solutions.

Aluminium oxide (Al_2O_3) solution was prepared on the day before and left stirring overnight. This solution contained 0.188g of $Al(NO_3)_3$, 5mL of MET and 0.075g of CH_4N_2O (urea was only introduced in the solution after 10min of stirring for the former reagents), achieving a concentration of 0.1M. After UV/Ozone substrate treatment, both ITO and silicon substrates were one-step spin-coated with 100µL of Al_2O_3 solution at 2000 rpm and for 35s. Next, substrates were placed inside the PSD PRO Series machine for 60min at 150ºC for thermal annealing. After the cooling of substrates, spin-coating and UV/heating processes were repeated, but at this time substrates only stood for 30min during PSD PRO heating.

Afterwards, all substrates were immersed in a 50mL isopropyl alcohol (IPA) solution with 0.787g of SA and sonicated for 10min with the purpose of diminishing future devices leakage current. This same solution, with all substrates in it, was left overnight with no sonication or heating process. Next, solution of IPA plus stearic acid was replaced by IPA only and left 10min sonicating in order to remove acid excess of all substrates. After ultrasonication, substrates were dried out with nitrogen gun and treated with UV/Ozone irradiation for 30min in order to increase surface energy and wettability, once again. This was the preparation process for perovskite one-step spin-coating.

As perovskite is unstable and photosensitive, laboratory temperature and humidity conditions were recorded during both solutions making and deposition [27,69]. Recorded averages were 24ºC and 60% of relative humidity.

Perovskite solutions were prepared on the day before and left stirring overnight. The four solutions contained the same amount of FAI (0.5mmol) and different amounts of $PbBr_2$ and PbI_2, fulfilling the molar ratio of 1:1 between FAI and the sum of $PbBr_2$ and PbI_2. Concerning only the sum of the latter precursors, the four solutions contained molar percentages of 5% plus 95%, 15% plus 85%, 25% plus 75%, and 50% plus 50% of $PbBr_2$ and PbI_2, respectively. Regarding this two used reagents, it is important to mention lead bromide was 40 times cheaper than lead iodide (fig.A1.3 on *Supporting information* appendix).

DMF and NMP solvents were added to solutions and with the same volume ratio of 4:1, respectively. As a result, all solutions contained a molar concentration of 1M.

After UV/Ozone substrate treatment, both ITO and silicon substrates containing two layers of Al_2O_3 were one-step spin-coated with 200µL of perovskite solution at an initial speed of 1000 rpm

for 10s and a second speed of 4000 rpm for 30s, during the same spinning program. An amount of 100μL of C_6H_5Cl (anti-solvent chlorobenzene), is deposited during the last 10 seconds of spinner motion in order to induce rapid crystallization of liquid perovskite solution.

This previous process occurred in a way to allow the coating of substrates (of same material) with different perovskite solutions. Meaning, at least four ITO substrates, all containing different perovskites, and the same way for silicon substrates.
Afterwards, all substrates were placed on a desiccator at 170ºC for 30min under vacuum conditions. This thermal annealing process allowed for crystalline grain size growth, resulting in homogenous, pinhole-free surface of solid perovskite.

Regarding substrate thickness, each Al_2O_3 layer is estimated to be 12nm [70] and for $FAPbBr_xI_{3-x}$ layers thickness will be discussed in chapter 3, *Analysis of results*.

Next, thin-films were attached to an aluminium mask for gold deposition, creating both source and drain gold contacts. After this stage thin-film transistors fabrication was completed (fig.2.1). For ITO-based MOS capacitors, layering structure was the same except for the upper-contact which was made of aluminium.

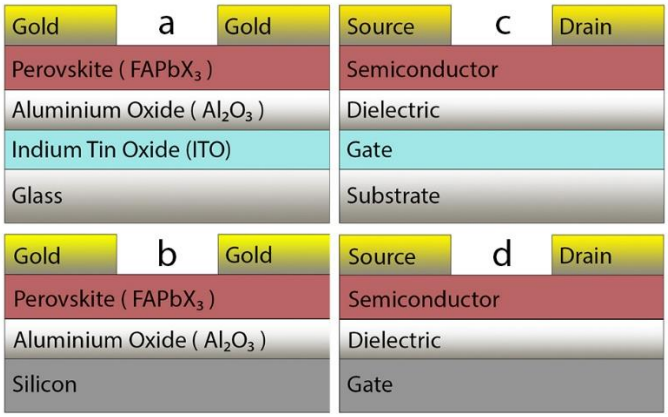

Figure 2.1 - a), b) ITO and silicon TFT fabrication, respectively. c), d) ITO and silicon TFT layer functions.

2.3 Material Characterization

Perovskite characterization occurred during the following stages: perovskite liquid solutions, perovskite-only substrates, films with aluminium oxide and perovskite, and finally substrates with aluminium oxide, perovskite and gold contacts (being TFTs).

Liquid perovskite solutions were sent to TGA-DSC STA 449 F3 Jupiter machine for thermogravimetric analysis (TGA) under natural atmospheric conditions, in order to study the effect of thermal annealing on different samples.

Perovskite-only silicon and ITO-based glass substrates were sent to SEM Hitachi TM3030Plus scanning electron microscope (SEM), Ambios X-200 profilometer, Perkin-Elmer Lambda 950 spectrophotometer and X´Pert PRO X-ray Diffraction (XRD) machine, in order to study films chemical composition, thickness, absorbance and crystal structure type, respectively.

ITO-based glass substrates with aluminium oxide and perovskite were tested at HL55WIN Hall system and Keysight B1500A machine, for charge carrier properties and capacitance-voltage profile analyses, respectively. To allow for measurements, films at this point were coated with aluminium dots, being the upper-contacts. ITO served as gate bottom-contact.

TFTs of both ITO and silicon substrates were sent to Agilent 4155C semiconductor parameter analyzer to perform output and transfer curves.

3 Analysis of Results

This chapter concerns all characterization data regarding $FAPbBr_xI_{3-x}$ solutions and devices. Results appear according to material complexity, from perovskite solutions to thin-film transistors.

Although $FAPbBr_2I_1$ based TFTs were not fabricated, these extra thin-films were produced in order to achieve a better understanding in film absorbance, thickness and morphology analysis, when varying bromine content. Films were fabricated in the same way as all the other $FAPbBr_xI_{3-x}$ perovskite thin-films.

3.1 Thermal Gravimetric Analysis

Before thermal gravimetric measurement (TGA), four $FAPbBr_xI_{3-x}$ solutions were heated at 70ºC for 3 days to remove solvent excess. After heating treatment, liquid samples transformed into a gel-type were sent for TGA and thermally examined under standard atmospheric pressure. In-situ x-ray diffraction was also developed for comparison with $FAPbBr_1I_2$ mass weight percentage, also in the same environmental conditions.

All four solution mass weights are inversely proportional to increasing temperature. Moreover, for relatively high temperatures, samples with higher bromine content retain more mass weight than those with lesser bromine content, also, this weight percentage difference between samples becomes larger with increasing temperature [71-73]. These results suggest that bromine addition to solutions provides a higher structure stability when considering thermal annealing processes of 80ºC or more. Plus, special attention is given to weight percentage at 170ºC as it was the chosen temperature for thermal annealing of all thin-films (fig.3.1a). This analysis confirms ion Br^- thermal stability already discussed in sub-chapter 1.2, *Perovskite materials*.

Regardless of mass weight, reagents such as PbI_2 can develop structure crystalline growth with increasing temperature and/or overtime, the same way perovskite structures do [69,74-76]. However, after structures reach their maximum peak around 250ºC, the number of crystal structures abruptly decreases for a mass weight of 90%, suggesting no direct relation between mass loss and crystalline growth (fig.3.1b).

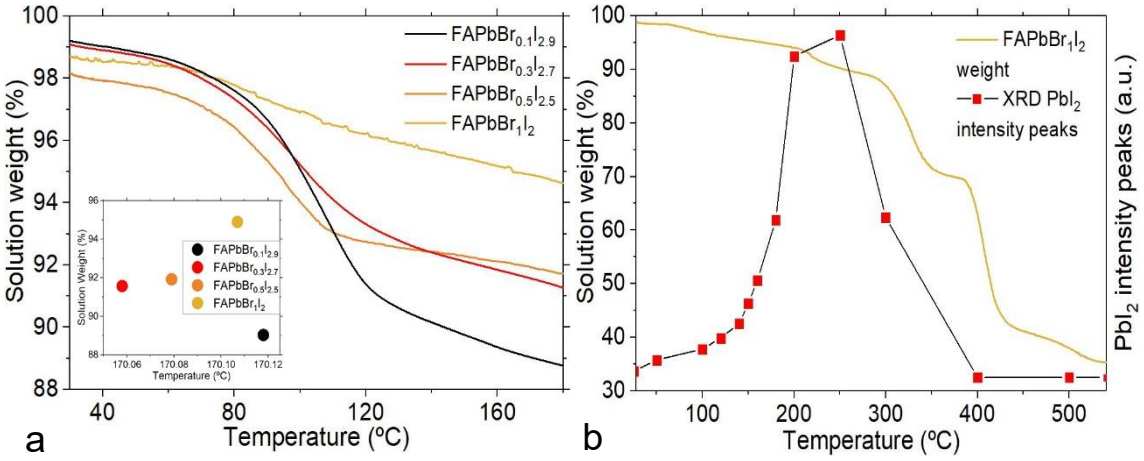

Figure 3.1 – a) Solution weight of samples with varied bromine content ($0.1 \leq x \leq 1$) as function of temperature heating. Inset graphic identifies more specifically weight percentage around 170ºC. b) Comparison between solution weight for and XRD impurity peaks for same $FAPbBr_1I_2$ sample, both as function of temperature annealing.

3.2 Energy-dispersive x-ray spectroscopy

Next to perovskite solution analyzes, thin-films were produced. In order to obtain a confirmation on samples chemical quantity, films were characterized via energy-dispersive x-ray spectroscopy (EDX) with SEM Hitachi TM3030Plus machine. Lead (*Pb*) and iodine (*I*) atomic percentages were collected. For bromine (Br), analysis was not possible because this element was inserted on a group of restricted elements for machine usage. Therefore, a ratio between atomic percentages of iodine and lead was made as an attempt for estimating bromine halide percentage in each sample. The expected bromine percentages were 3.33%, 10%, 16.67%, 33.33% and 66.67% for $FAPbBr_{0.1}I_{2.9}$, $FAPbBr_{0.3}I_{2.7}$, $FAPbBr_{0.5}I_{2.5}$, $FAPbBr_1I_2$ and $FAPbBr_2I_1$, respectively.

According to EDX data from recent literature, an inversely relation between the ratio of *I* and *Pb* atomic percentages and present bromine quantity is verified [77-78]. In the light of this suggestion, all produced films with lesser bromine quantity had lower bromine halide percentages than the expected (2.17%, 9.5%, 13% and 28.33% instead of 3.33%, 10%, 16.67% and 33.33%, respectively). The only exception was for the film with higher bromine content, having more percentage than the theoretically expected (72.89% instead of 66.67%) (fig.3.2).

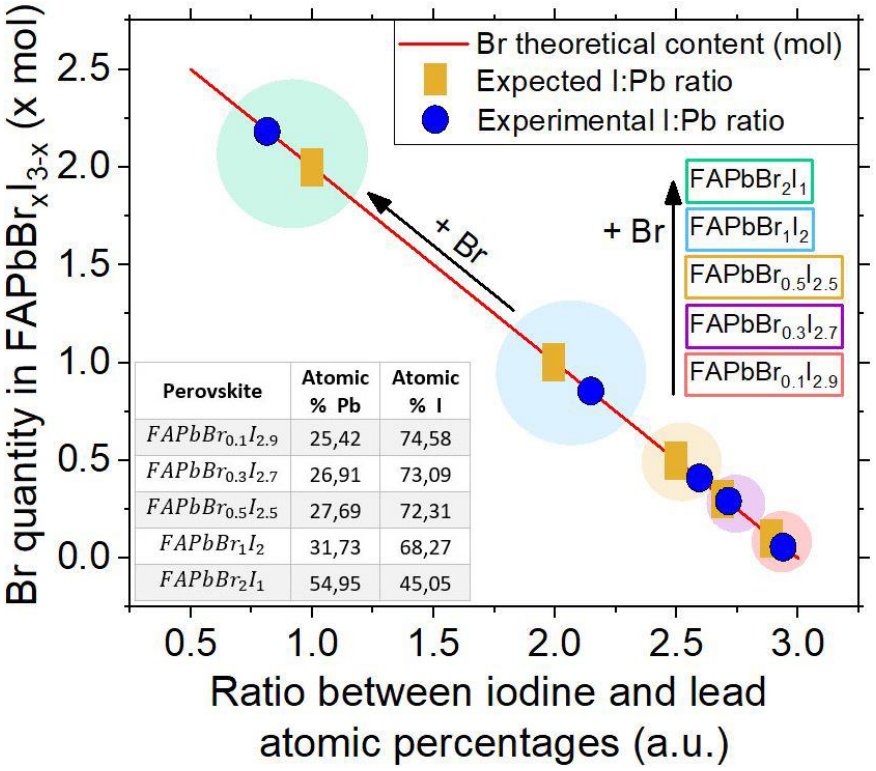

Perovskite	Atomic % Pb	Atomic % I
$FAPbBr_{0.1}I_{2.9}$	25,42	74,58
$FAPbBr_{0.3}I_{2.7}$	26,91	73,09
$FAPbBr_{0.5}I_{2.5}$	27,69	72,31
$FAPbBr_1I_2$	31,73	68,27
$FAPbBr_2I_1$	54,95	45,05

Figure 3.2 – Bromine halide percentage in $FAPbBr_xI_{3-x}$ as a function of theoretical and experimental iodine - lead atomic percentage ratios. The blue dots represent the obtained samples and the orange rectangles are the ideally expected atomic ratio, and therefore the ideal bromine quantity. Both these symbols are surrounded by circles, each circle is related to a different perovskite composition. Inset table shows the experimentally obtained table by EDX analysis.

3.3 Absorbance analysis

Perovskite-only ITO-based glass thermal annealed substrates were subjected to absorbance and bandgap measures, calculated using transmittance data from Perkin-Elmer Lambda 950 spectrophotometer. Absorbance was directly obtained by Perkin Elmer machine and optical bandgap results were estimated using Tauc Plot method [79-82] for direct bandgap semiconductors [83-84]. Obtained results agreed with recent perovskite literature.

Regarding $FAPbBr_xI_{3-x}$ samples, all absorbance results demonstrate higher inconsistency at lower wavelengths ($350nm \leq \lambda \leq 440nm$) and smaller peaks when increasing bromine content [85-86]. However, the latter films seem to retain a higher level of absorbance at bigger wavelengths ($440nm \leq \lambda \leq 600nm$) (fig.3.3a). Plus, absorbance results at ($\lambda = 600nm$) stabilize for ($600nm \leq \lambda \leq 2000nm$).

When increasing bromine content to x = 2 ($FAPbBr_2I_2$) absorbance stability increases among samples and peaks at lower wavelengths also slightly increase. Moreover, it's possible to conclude that absorbance increases after thermal annealing process [87-88], meaning samples become denser (fig.3.3c).

Optical bandgap calculations for $FAPbBr_xI_{3-x}$ suggest film surface divergences, as according to literature data, three structure types were identified [89]. Regarding films tolerance factor and as explained in Introduction chapter, hexagonal structures suggest (t higher than 1), cubic structures (t around 1), tetragonal and orthorhombic structures (t lower than 1). Therefore, these films tolerance factor will be different from theoretical values presented in *Introduction* Chapter.

Bandgap counting indicates the presence of mostly hexagonal structures ($2eV \leq Eg \leq 2.5eV$) which can be related to environment humidity [90-91], also, some of these twelve samples present two absorbance peaks (dual phase), possibly suggesting varied film thickness and therefore confirming the presence of more than one structure types. This may be related to precursors inadequate mixing during deposition process [65] (fig.3.3b).

For $FAPbBr_2I_1$ samples, results are quite different. Regardless of thermal annealing process, all eight samples present a dual phase which seem to correspond to orthorhombic structures ($1.2eV \leq Eg \leq 1.45eV$) and cubic structures ($1.85eV \leq Eg \leq 1.65eV$) [89].

As PbI_2 reagent was not used to produce $FAPbBr_2I_1$ films, solution purity increased and risk of contamination diminished, also, more bromine incorporated seems to stabilize absorbance results. One of these reasons, or maybe both, is probably related to the equal quantity of present structures in $FAPbBr_2I_1$ films. Concerning thermal annealing, optical bandgaps slightly diminish after this process. (fig.3.3d).

Compared to recent literature, samples with lower bromine quantity ($0.1 \leq x \leq 1$), present an absorbance profile similar to those of lead halides [92], $MAPbI_3$ ambipolar hybrid phototransistors [93] and $MAPbI_3$ solar cells [94]. Furthermore, for all samples ($0.1 \leq x \leq 2$), as a bandgap increase is probably related to film polycrystallinity, films with lower bromine content ($0.1 \leq x \leq 1$) are likely to have a higher number of polycrystalline structures when compared to $FAPbBr_2I_1$ sample structures [95].

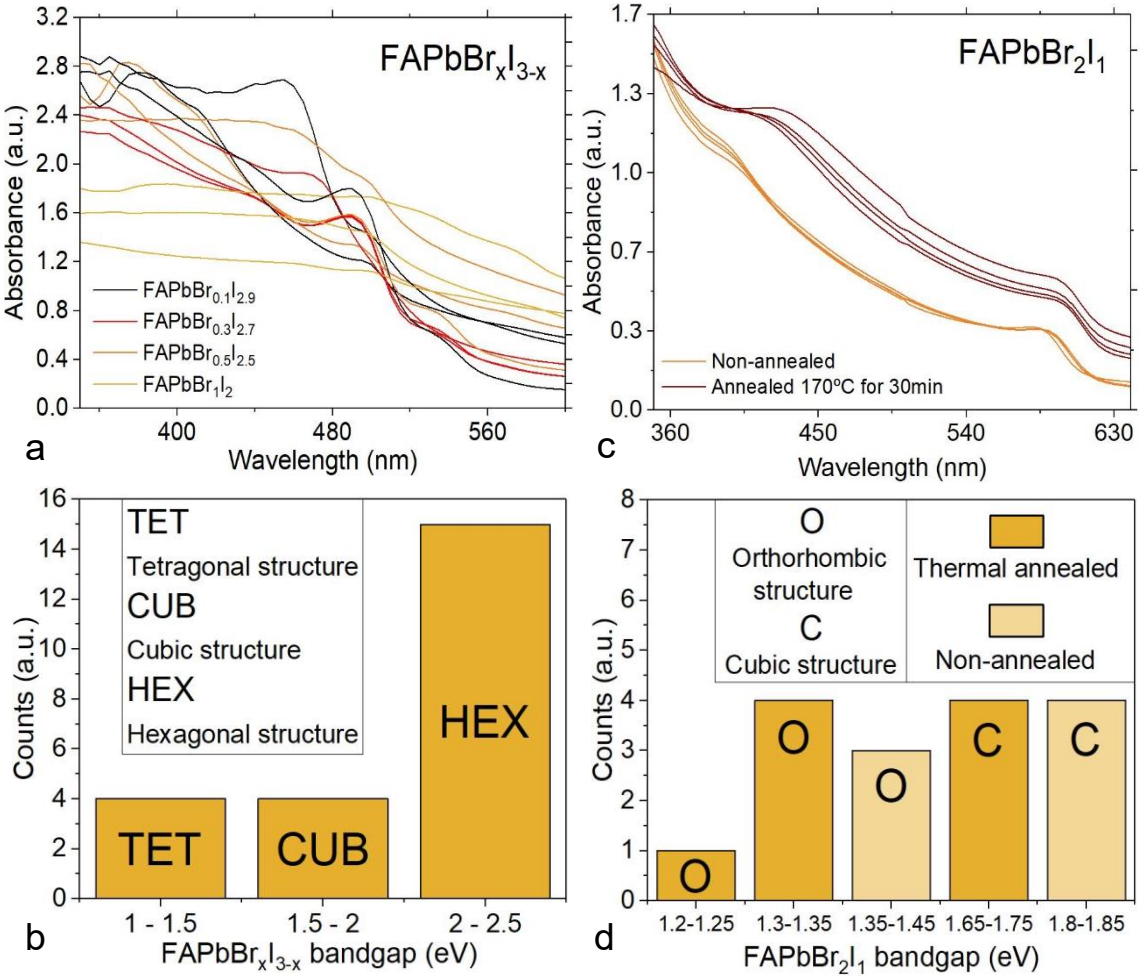

Figure 3.3 - a), c) Absorbance of $FAPbBr_xI_{3-x}$ and $FAPbBr_2I_1$ samples as function of light wavelength. b, d) $FAPbBr_xI_{3-x}$ and $FAPbBr_2I_1$ tauc plot bandgap counting and identification of formed structures, according to literature.

3.4 Thickness measurement

Perovskite-only ITO-based glass thermal annealed substrates were thickness-analyzed by Ambios X-200 profilometer. Regarding films deposition, a small piece of kapton tape was added before spin-coating process to create one height step between substrate and perovskite film, thus facilitating profilometer measurement. Moreover, Swanepoel's method of envelopes was introduced using Perkin Elmer transmittance data to estimate films thickness [96-98].

According to profilometer results, average thickness tends to increase for films with higher bromine content, which is in accordance with solar cells literature [99]. All films show thickness uncertainty regardless of bromine content, which can be related to the number of structure types present in samples, as discussed in *Absorbance analysis* sub-chapter. It is also important to refer that this uncertainty increases for samples with few bromine quantity, and then it gets smaller when adding a considerable amount of this cation (fig.3.4).

When comparing $FAPbBr_{0.1}I_{2.9}$ group of samples to the other groups, its uncertainty height is an exception, and this is probably due to the very low chemical quantity of present bromine, which is not enough to form bromine-based perovskite structures. This way less structure types are formed and thickness uncertainty decreases.

Regarding thickness calculation by transmittance data, the lowest calculated value from bottom envelops was 150nm and the highest value 296nm by upper envelops, establishing an estimate thickness region in accordance with the lower half of all profilometer thickness uncertainty bars.

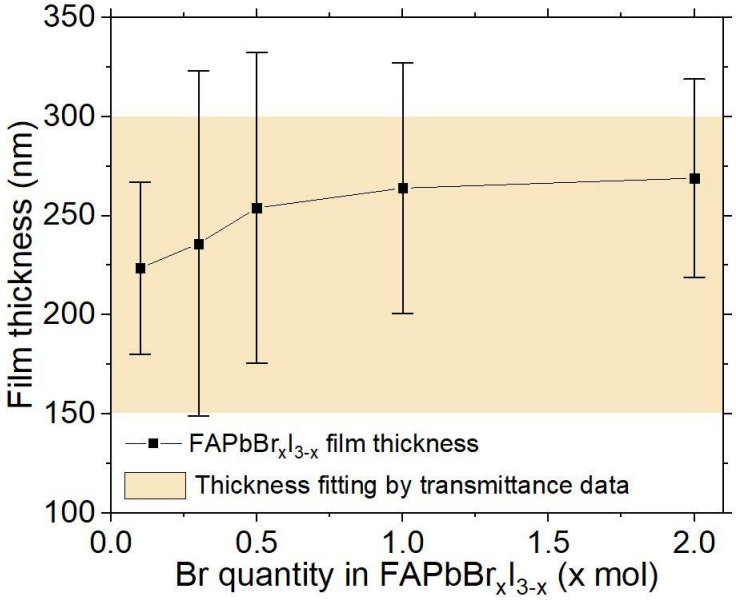

Figure 3.4 - Film thicknesses of $FAPbBr_xI_{3-x}$ samples as function of bromine content ($0.1 \leq x \leq 2$). Brown rectangle represents Swanepoel's thickness fitting [96-98].

3.5 X-ray Diffraction

Perovskite-only ITO-based glass and silicon thermal annealed substrates were sent for x-ray diffraction (XRD) to analyze films crystallinity and purity. ITO-based substrates were all produced on the very same conditions, using same deposition process and a thermal annealing of 170ºC for 30min under vacuum. In-situ XRD technique was utilized to study samples thermal annealing process by varying time and temperature. Lastly, perovskite-only silicon-based substrates were also tested at XRD and used to compare films with different thermal annealing conditions.

3.5.1 ITO-based samples

When increasing bromine contents, it's possible to identify a general horizontal peak shift and this is because bromine has a smaller lattice parameter than iodine, which shifts crystal structure peaks to higher angles [77]. Moreover, all $FAPbBr_2I_1$ peaks have lesser values of full width at half maximum (FWHM), meaning a higher number of crystal structures with a more precise lattice parameter (fig.3.5a).

Regarding XRD between 11º and 15º, two peaks are identified for x = 0.1. One very precise peak at 11.8º, which is related to perovskite yellow phase regarding hexagonal structures, and another peak around 12.6º suggesting the existence of PbI_2 impurities [77,100] (corresponding to δ_{H} and I symbols in fig.3.5, respectively). When adding few more bromine, yellow phase disappears, PbI_2 impurities increase and $PbBr_2$ precursor reacts with part of PbI_2, which is visible around 11.6º. The latter event suggests that, if both reagents react to each other only ($PbBr_1I_1$) [101-102], a similar sized FAI impurity, around 13º [103], also appears confirming a low or non-existent number of $FAPbBr_xI_{3-x}$ crystalline structures. However, when increasing bromine to x = 2, FAI and $PbBr_1I_1$ impurities completely disappear, PbI_2 impurity nearly disappears, and black phase (a_{C} symbol in fig.3.4) regarding cubic $FAPbBr_xI_{3-x}$ structures appears around 14.6º [77]. For x = 1, it was already possible to identify a black phase small peak around 14.3º (fig.3.5d).

In order to prove the diminishing of impurities, a sum of all impurity peaks intensity between 11º and 15º has been made as a function of bromine concentration (fig.3.5b).

XRD peaks between 20º and 40º were also specifically analyzed. It's possible to visualize a gradual decrease in hexagonal phase and PbI_2 impurity peaks (symbols) when increasing bromine content [77]. For x = 2, cubic or pseudo-cubic perovskite structures appear, PbI_2 impurity totally or nearly disappears and a relatively small $PbBr_2$ impurity (Br symbol in fig.3.4) forms around 20º. ITO peaks (* symbol in fig.3.4) don't change much with bromine concentration, and,

just like all identified peaks written above, are in accordance with recent literature [77,104-106] (fig.3.5c).

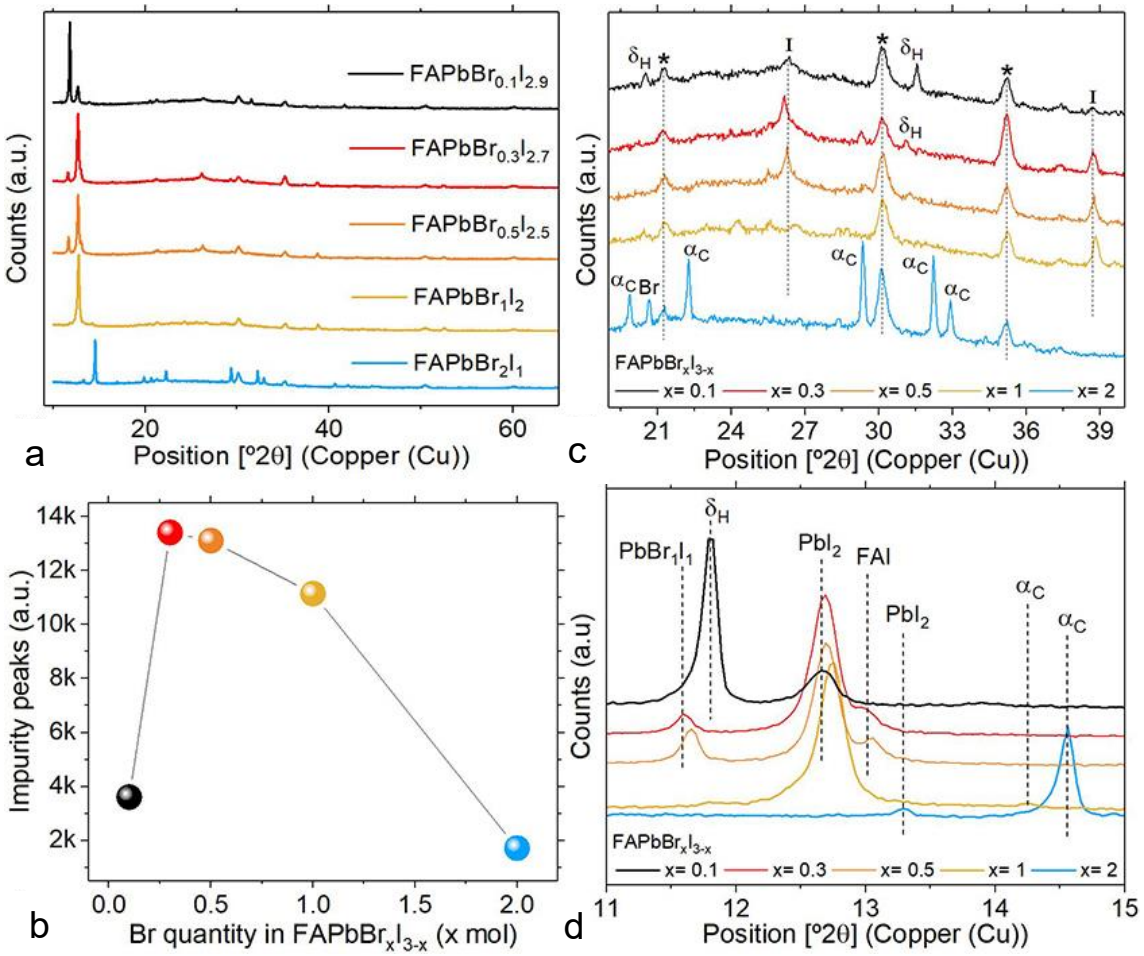

Figure 3.5 - a) X-ray diffraction of $FAPbBr_xI_{3-x}$ samples with varied bromine content ($0.1 \leq x \leq 2$). b) Recorded intensity peak impurities in the range of $11 \leq 2\theta \leq 15$. c), d) X-ray diffraction zoom-in for same $FAPbBr_xI_{3-x}$ samples, concerning ranges of $20 \leq 2\theta \leq 40$ and $11 \leq 2\theta \leq 15$, respectively.

3.5.2 In-situ XRD

One perovskite-only silicon-based $FAPbBr_1I_2$ sample was sent for In-situ XRD in order to study both annealing time and temperature effects on crystallinity rate.

Sample was subjected to a non-vacuumed annealing of one hour per temperature, obtaining four XRD measures per hour and measuring along thirteen temperature levels within the range of 50ºC to 600ºC. For each temperature, first three measures were obtained during the first 30 minutes and the fourth measure was taken 30 minutes after the third measure (fig.3.6b).

Regarding all fifty-two measures, highest recorded intensities over time can be observed in fig.3.6a.

Concerning the highest peak, PbI_2 impurity around 12.6º [77,100], annealing temperatures from 50ºC to 200ºC present higher intensity during their fourth measure, meaning temperature-time profile is appropriate until 200ºC. However, an increase in temperature ($T \geq 250ºC$) confirms a gradual downfall on PbI_2 crystallinity, taking place right after the appearance of the highest over-time recorded peak. The latter peak was obtained at 250ºC for 10 minutes, suggesting that similar temperature-time profiles should finish at this point, achieving the highest possible crystallinity (fig3.6c).

Moreover, another relevant XRD peak is identified near 68º with an increasing intensity proportional to temperature during all temperature-time profile. This peak, which was not identified for ITO-based glass $FAPbBr_1I_2$, suggests a silicon-based structure as it was no target of thermal degradation, actually the opposite [107-110]. Increasing intensity after measure number 40 is related to the appearance of this structure (fig.3.6a, d)

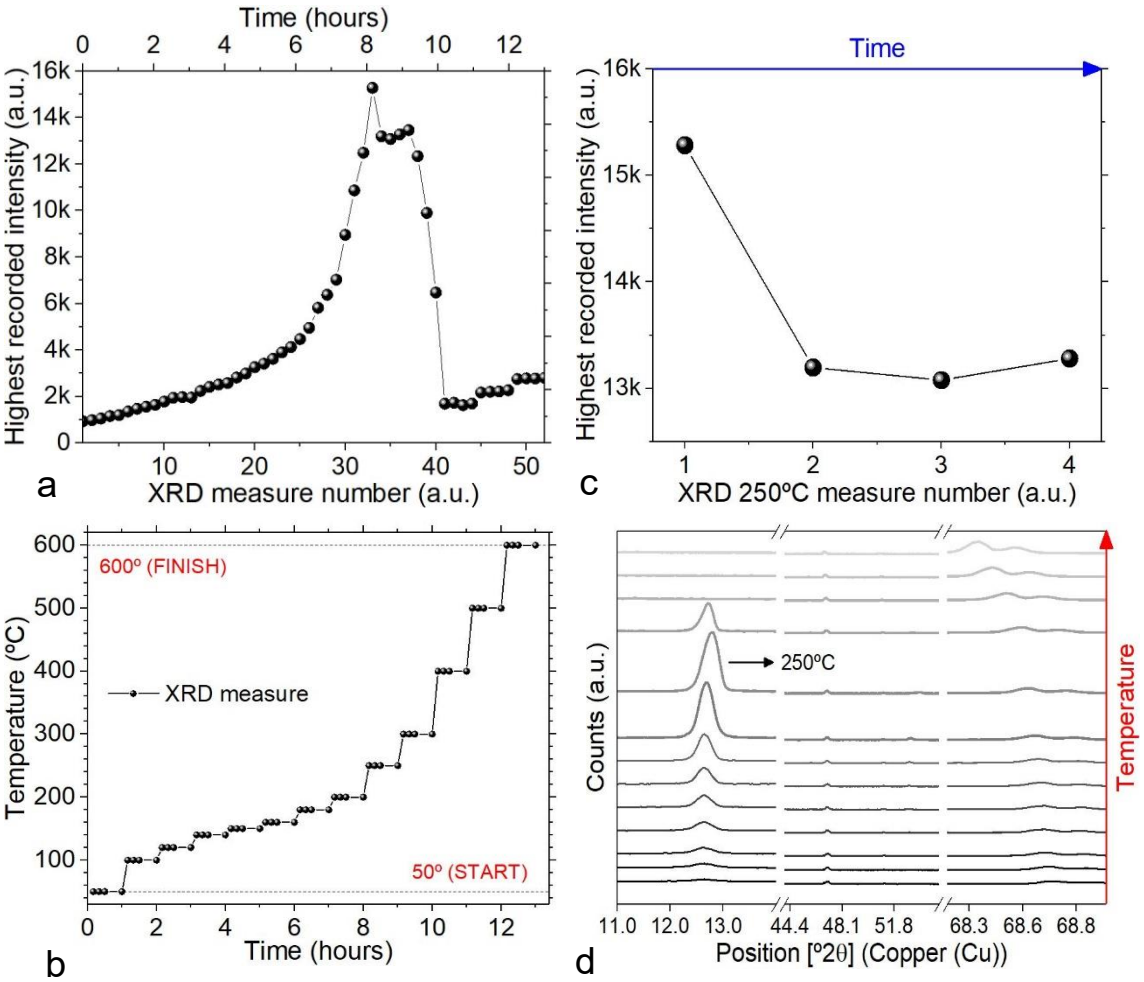

Figure 3.6 – a) XRD recorded intensity peaks during full temperature-time profile, obtaining a total of 52 measures. b) Temperature profile as function of sample thermal annealing. c) XRD recorded intensity peaks for 250ºC. d) XRD relevant 2θ positions vertically displaced as both intensity and annealing temperature functions.

3.5.3 Silicon-based samples

Silicon-based $FAPbBr_1I_2$ films were analyzed in order to study the effect of thermal annealing conditions in perovskite crystallinity. Silicon substrate was used instead of ITO-based glass to collect more results, also allowing for silicon and ITO comparison.

According to XRD results, samples annealed under vacuum conditions develop higher crystallinity and peaks with lesser FWHM [111-112], meaning a higher number of crystalline structures and with very similar lattice parameters. Plus, an inexistent peak at ITO-based $FAPbBr_1I_2$ appears around 60º for both silicon samples, suggesting a silicon-related crystal structure (fig.3.7a) [107-110].

Regarding XRD between 12.3º and 13.1º, both peaks suggest the existence of PbI_2 impurity, as observed in ITO-based $FAPbBr_1I_2$ sample [77]. The horizontal shift concerning the non-vacuumed sample is probably related to precursors sensitivity to humidity, which according to perovskite literature is higher for iodine than bromine (fig.3.7c) [113].

Concerning silicon films, pictures were taken to both samples, vacuumed and non-vacuumed. A darker tone of color is observed for the vacuumed sample, which suggests a relation between film color intensity and crystallinity (fig.3.7b, d).

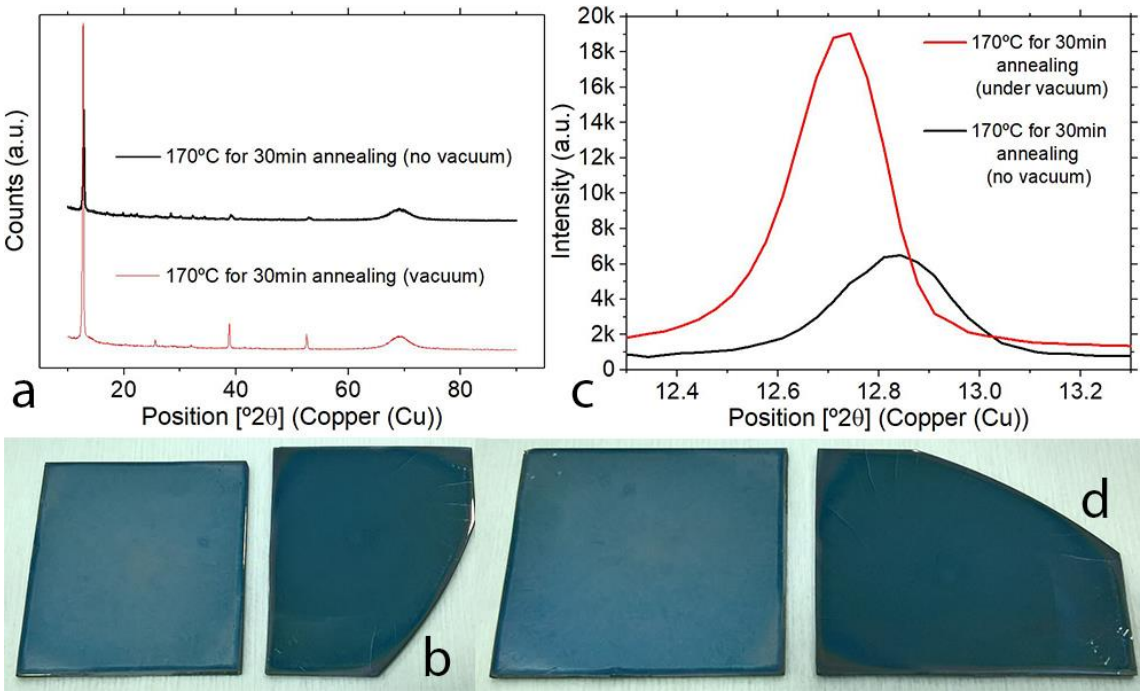

Figure 3.7 – a) Overall XRD profile comparison between vacuumed sample (red line) and non-vacuumed sample (black line). c) XRD zoom-in on $12.3º \leq 2\theta \leq 13.3º$ regarding PbI_2 impurity peaks for both samples. b), d) Surface colorimetric differences between both samples, suggesting an overall darker tone for the vacuumed sample.

Regarding silicon samples, standard annealing process was also compared to In-situ annealing. Two silicon based $FAPbBr_1I_2$ samples, both annealed under standard atmospheric pressure, were subjected to different annealing treatments and place side by side at XRD examination.

Visualizing XRD graphics, it´s possible to detect two higher peaks around 12.7º which concerns same PbI_2 impurity already discussed (fig.3.8b) [77,100]. This impurity represents the only peak lower for In-situ XRD sample when compared to standard annealed sample, as all the other peaks are more intensive and have lesser FWHM for the In-situ case (fig.3.8a).

Moreover, a horizontal shift to higher angles happens for standard annealed sample which is probably related to silicon substrate, as ITO-based samples subjected to the same standard process don't present these shift on peaks with this level of intensity. These results suggest silicon possibly requires more annealing time than ITO-based glass substrates (fig.3.8b, c, d).

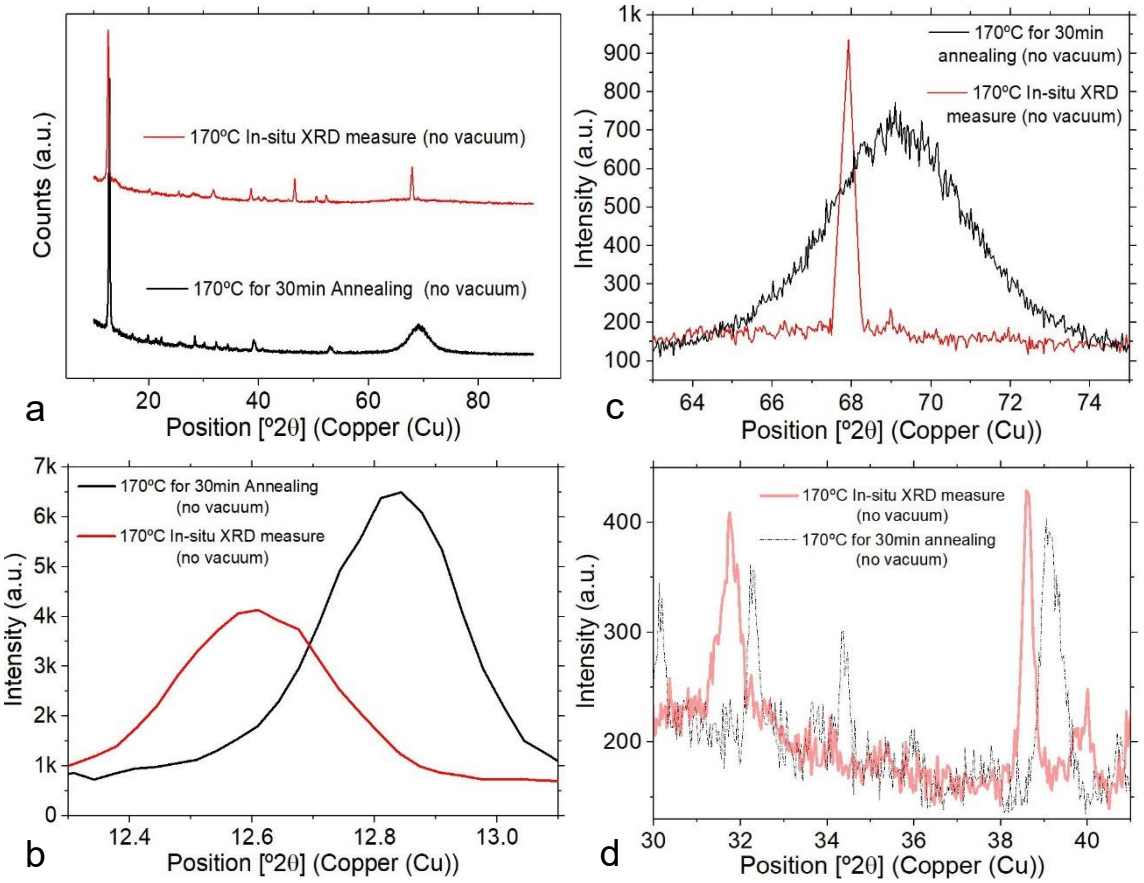

Figure 3.8 – a) XRD peaks comparison between standard annealing and In-situ XRD annealing of $FAPbBr_1I_2$ samples. b), c), d) XRD zoom-in for both samples regarding peaks within the ranges of $12.3º \leq 2\theta \leq 13.1º$, $65º \leq 2\theta \leq 75º$ and $30º \leq 2\theta \leq 41º$

Overall, impurities and degradation verified for some ITO and silicon samples, are possibly related to the effective time used for thermal annealing process, as pointed out by one research concerning annealing effects on $FAPbI_3$ solar cells [114]. Plus, and regarding ITO samples only, the contrasting thermal expansions of perovskite and Indium-tin oxide can contribute to a faster perovskite degradation [115].

3.6 Charge-carrier properties

ITO-based glass samples with semiconductive and conductive layers, perovskite ($FAPbBr_xI_{3-x}$) and aluminium coverage, respectively, were tested at HL55WIN Hall effect machine for charge-carrier properties analysis. Values of carrier concentation, mobility and resistivity were obtained for films with different bromine contents ($0.1 \leq x \leq 1$). Due to program error, some mobility and resistivity values were not recorded by the computer. Yet, all charge concentration values either n-type or p-type were properly displayed.

According to concentration data, p-type nature is identified for $FAPbBr_{0.1}I_{2.9}$ and $FAPbBr_{0.5}I_{2.5}$ samples, whereas n-type is obtained for all studied samples. It's possible to conclude that, for low bromine content ($x = 0.1$), all concentration values present very large mean deviation, meaning an overall divergence from both n-type and p-type averages. Increasing bromine content ($x \geq 0.1$) results in much higher concentration averages and lesser mean deviations. Moreover, for sample $FAPbBr_{0.5}I_{2.5}$ n-type and p-type concentrations are very similar suggesting ambipolar characteristics (charge transport of both electrons and holes), as positive and negative values were obtained in different trials for the same thin-film (fig.3.9a).

Regarding data with associated resistivity and mobility, all resistivity values diminish when increasing bromine to $x = 0.3$ and stabilize for $0.3 \leq x \leq 1$. Mobility values increase with ascending bromine content. These values, being very similar for both n-type and p-type mobilities, also suggest sample ambipolarity and are relatively high when compared to recent perovskite literature (fig.3.9b). The latter describes a recorded maximum p-type mobility of $15 cm^2/Vs$ and n-type mobility of $27 cm^2/Vs$ for polycrystalline thin-films produced in the very same conditions and materials [116-118]. Plus, for relatively similar perovskites ($(FAPbI_3)_{1-x}(MAPbBr_3)_x$), p-type and n-type mobilities of $20 \pm 8\ cm^2/Vs$ and $17 \pm 9\ cm^2/Vs$, respectively, were presented in another research [119]. In this work, maximum achieved mobilities were $20.2 cm^2/Vs$ for p-type and $38 cm^2/Vs$ for n-type.

Overall, here all studied concentration, mobility and resistivity properties stabilize for higher bromine contents ($x \geq 0.1$). All recorded hall mobility values suggest the presence of mostly polycrystalline structures, as single-crystal mobility is generally 10 times higher (or more) than the former structures [120-121].

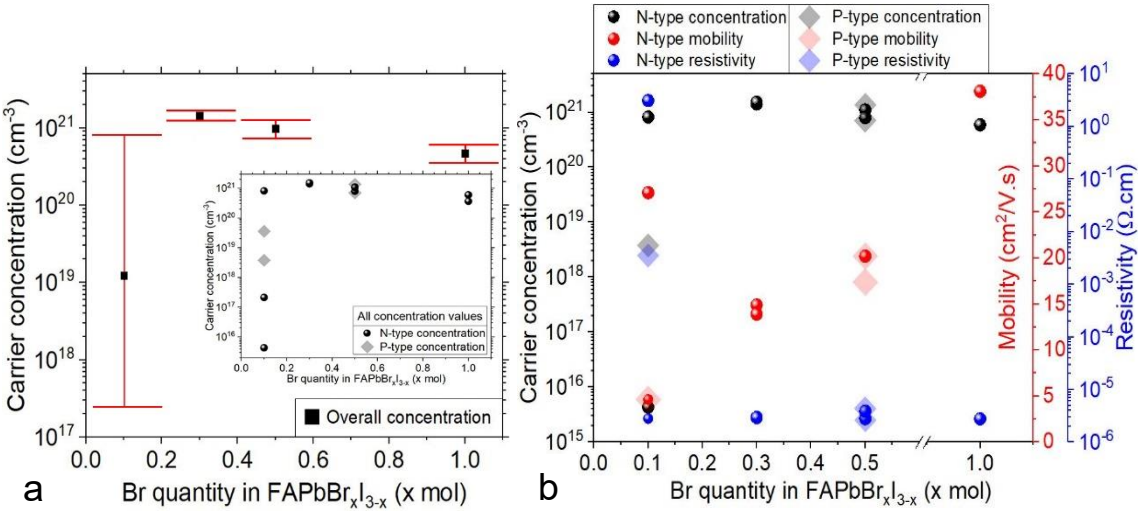

Figure 3.9 – a) Charge concentration with bromine content variation. b) Thin-flms associated carrier mobility, resistivity and charge concentration.

When obtaining hall mobility, structural information such as thin-film crystalline nature can be estimated by calculating diffusion coefficient D_C. The latter coefficient is directly obtained from the recorded mobility, and when multiplied by the average carrier lifetime (defined as the time a minority charge takes to recombine) it provides the squared value of average carrier diffusion length, the distance completed by a particle before its recombination with a carrier of the opposite charge. For the following analyses, $FAPbBr_{0.1}I_{2.9}$ sample with n-type hall mobility of $27.1 cm^2/Vs$ is assumed to be one $FAPbI_3$ substrate, because mobility value is exactly the same according to literature [116], and, as discussed in *Absorbance analysis* and *X-ray diffraction* sub-chapters, films with very low bromine content have higher chances of not developing any bromine structures at all.

Diffusion coefficient values were obtained directly from hall mobility, whereas carrier lifetime, that can be analyzed via time-resolved photoluminescence spectroscopy [122], was not done during laboratory work. Therefore, using literature information on $FAPbX_3$ carrier lifetime t_C and diffusion length D_L, theoretical diffusion coefficients were calculated using organic semiconductor formula ($D_L = \sqrt{D_C t_C}$) and related to D_C values obtained during this work. Plus, as single crystal and polycrystalline films generally present different carrier lifetime t_C (and therefore different diffusion lengths) [123], literature information was also compared to thin-film coefficients as an attempt to understand the crystalline structures of films developed in this work.

Interestingly, when increasing bromine content, experimental diffusion coefficients approach a theoretical $FAPbX_3$ single-crystal profile instead of polycrystalline profile, according to the suggested carrier lifetime ranges (usually $100ns \leq t_C \leq 1000ns$ for polycrystalline and $400ns \leq$

$t_C \leq 4000ns$ for single-crystal). Furthermore, when relating the diffusion coefficient D_C of $FAPbI_3$ ($D_C = 0.70cm^2/s$, for sample with $27cm^2/Vs$ mobility) with theoretical carrier lifetime, a diffusion length of $6.45um$ is achieved which is similar to single-crystal's $FAPbI_3$ literature data of about $6.60um$ (fig.3.10a) [124]. These results are the opposite of those suggested by hall mobility. Probably meaning that, samples are for all purposes, polycrystalline, however displaying single-crystal characteristics such as higher carrier lifetimes and diffusion lengths [125].

Moreover, and according to recent literature, an inversely relation between carrier mobility and lifetime is verified for organic photovoltaics. This information can probably contradict the previous conclusions on samples crystal structures, as obtained polycrystalline hall mobilities are relatively high and therefore the respective carrier lifetimes would be low [126]. However, this is not conclusive as another study, based on halide perovskites, suggests a direct relation between carrier lifetime and thermal annealing time [122]. Samples for this work were annealed during 30min, which is considered a relative high time.

According to time-of-flight method for organic semiconductors, thin-film charge transit time (the time device takes to respond) can be obtained when knowing the values of carrier mobility and separation distance between contacts [127-129]. Therefore, mobility values were obtained and the distance between the four electrodes was verified to be the same during all measurements, of about 1cm. Along with transit time calculations, another studied factor was the hall contact voltage, resulting as a voltage average measured between all the contacts. Concerning this data, when lifting carrier mobility (either n-type or p-type), charge transit time diminishes and average contact voltage increases (fig.3.10b).

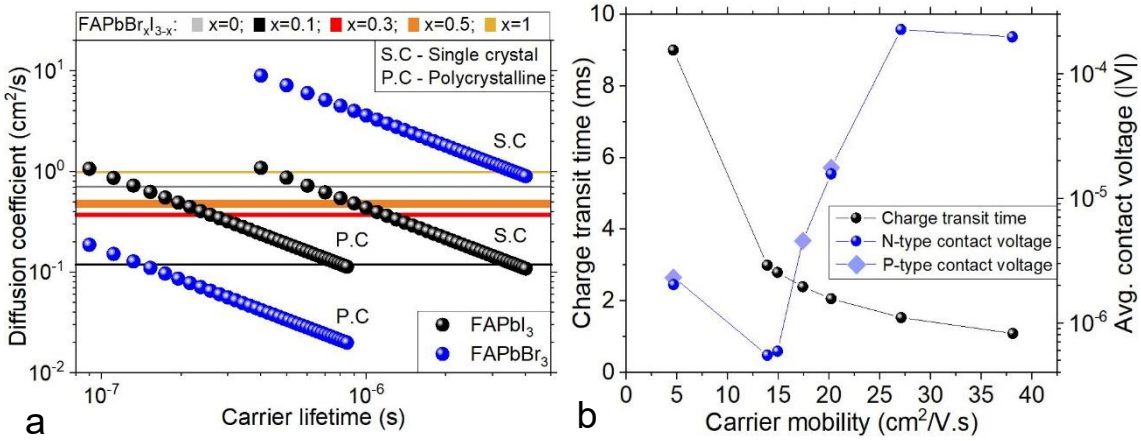

Figure 3.10 – a) Comparison between diffusion coefficient values directly obtained from hall effect mobilities (horizontal bands) and diffusion coefficient values of literature data (FAPbI3 being the black dots and FAPbBr3 the blue dots), providing a relation between carrier diffusion and expected range of carrier lifetime for both single crystal and polycrystalline films [123-124]. b) Charge transit time and average hall contact voltage, both as a function of carrier mobility [127-129]

3.7 Capacitance measurement

ITO-based glass metal-oxide-semiconductor (MOS) capacitors with dielectric, semiconductive and conductive layers, aluminium oxide (Al_2O_3), perovskite ($FAPbBr_xI_{3-x}$) and aluminium coverage, respectively, were tested at Keysight for capacitance analysis.

Concerning voltage terminals, a small thin-film area was covered with kapton tape during layers deposition in order to allow ITO intact gate surface. Perovskite coverage with small aluminium dots was made for creation of the source, the upper contact. Since data errors occurred for some of the measurements, probably due to leakage current or bad electrical contact, only $FAPbBr_{0.1}I_{2.9}$ and $FAPbBr_{0.5}I_{2.5}$ samples were successfully analyzed.

Regarding data, capacitance-voltage profile and capacitance minimums on capacitance-frequency forward bias suggest the presence of negative capacitance phenomenon (fig.3.11a, c, d) [130-132]. Halide content variation doesn't seem to influence any of these profiles, only the overall capacitance increases with decreasing bromine quantity (fig.3.11c, d). Also, relative to halide content, thin-film absorbance profiles of this work look similar to literature absorbance of $MAPbI_{3-x}Cl_x$ MOS capacitor, supporting data of *Absorbance analysis* sub-chapter [133]. All present capacitance-voltage sweeps were made using 1 kHz frequency.

Moreover, concerning photosensitivity of $FAPbBr_{0.1}I_{2.9}$ MOS capacitor, capacitance-voltage profiles are relatively similar for both light and dark conditions (fig.3.11c).
According to recent literature, iodine ions can flow among crystalline grains under an applied bias, and the boundaries of these grains dominate a phenomenon known as ion migration [133].

These samples possess negative capacitance probably due to ion migration, suggesting film and surface instability that could partly explain for absorbance and thickness data uncertainties (figs. A1.5 and A1.6 on *Supporting information* appendix) [134]. Based on this information, and according to recent literature, ion migration is directly related to strange photoelectrical behaviors in polycrystalline solar cells, but not in single-crystal cells [135], thus, supporting the assumption in *Charge-carrier properties* sub-chapter about films polycrystalline nature.

Negative capacitance can happen for a wide range of frequencies (10^{-4} kHz - 10^{2} kHz). This phenomenon is usually related to poor photovoltaic conversion efficiency as it develops deleterious effects in solar cells [136]. However, transistors made with negative capacitance are a recent object of study regarding low-power consuming electronics [137]. Therefore, thin-films fabricated specifically for solar cells that gain these properties should not be put aside, but sent for potential analysis within other devices instead.

Along capacitance-voltage curves, current-voltage sweeps were also made to analyze possible leakage current. According to results, samples with lesser bromine had much higher current levels, indicating lesser chance of leakage when increasing bromine content (fig.A1.7 on *Supporting information* appendix).

Moreover, a graphic with inversed squared capacitance as function of gate voltage forward sweep was also made in order to study slope profile. This slope also known as Mott-Schottky slope, provides direct information about the nature of present charges, electrons or holes. For a specific gate voltage sweep direction, either forward or reverse sweep, a positive slope suggests the presence of acceptor particles, meaning hole charges, while a negative slope is related to donor particles also known as electron charges [138-141]. Charge-carrier concentration and built-in potential (voltage) can also be obtained for a linear Mott-Schottky plot, however, in this case, inversed squared capacitance data demonstrated an exponential profile, becoming impossible to achieve accurate linear fitting.

Nevertheless, slope profile was successfully analyzed. Both positive and negative slopes were identified, regardless of bromine content or positive/negative voltage. $FAPbBr_{0.1}I_{2.9}$ data majority identifies a very consistent positive slope for data between -1V and 0.2V, and a small data collection suggests a possible negative slope for data between 0.2V and 0.3V. $FAPbBr_{0.5}I_{2.5}$ data is more balanced in terms of slope nature, as one half of total collected data suggests the presence of two negative slopes, (data from -1V to -0.6V and 0V to 0.5V), and the other data half, between -0.6V and 0V, identifies a consistent positive slope similar to $FAPbBr_{0.1}I_{2.9}$ p-type slope (fig.3.11b).

Regarding the explained Mott-Schottky data, an increase in bromine allows for a more balanced data between p-type and n-type nature, this way suggesting higher ambipolar characteristics for higher bromine contents. These results are in accordance with hall effect analysis in *Charge-carrier properties* sub-chapter.

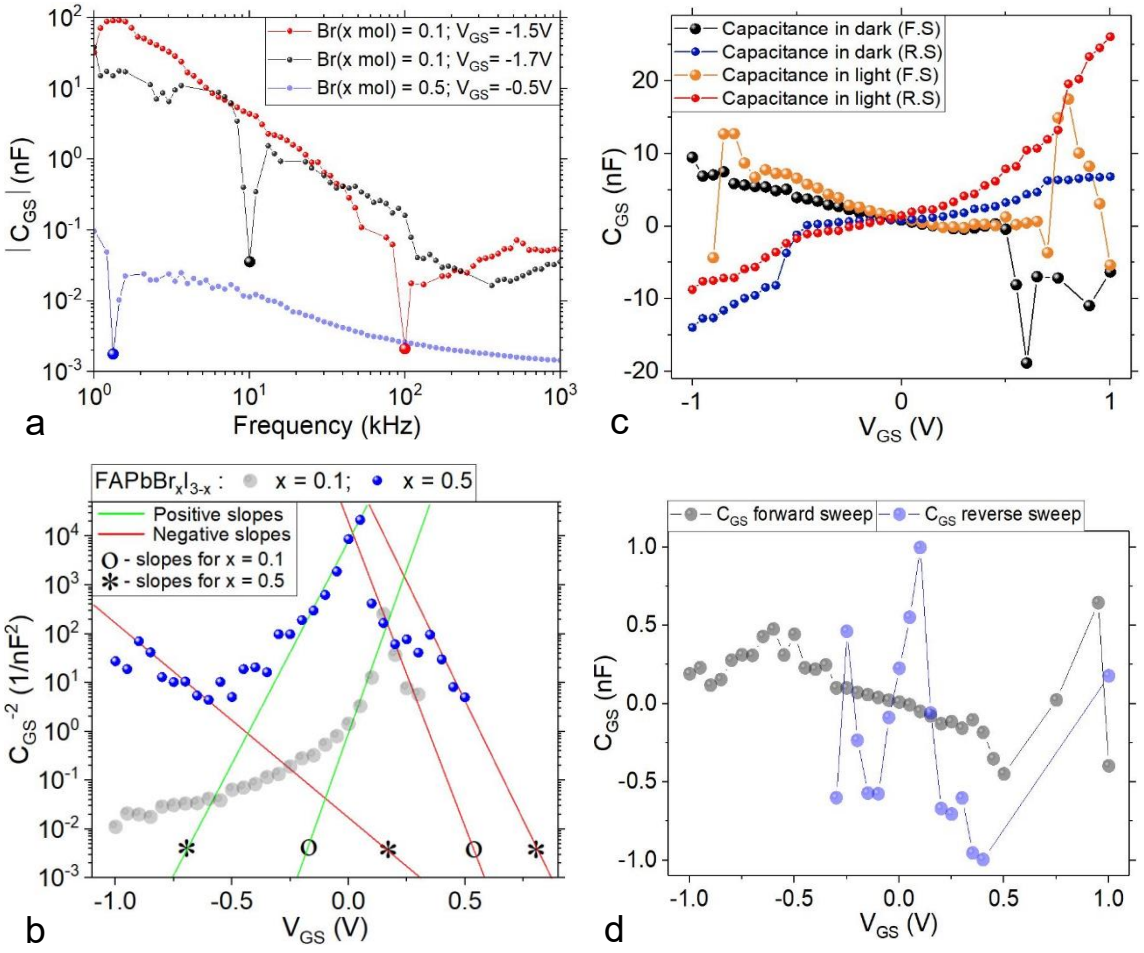

Figure 3.11 – a) Generic capacitance-frequency forward bias in dark, b) inverse squared capacitance for mott-schottky slope analysis, c) capacitance-voltage (CV) sweeps under dark and light conditions for same bromine content x = 0.1 using 1kHz frequency, and d) CV sweep in dark for bromine quantity x = 0.5 using 1kHz frequency.

3.8 Transistor performance

ITO-based glass and silicon samples with dielectric, semiconductive and conductive layers, Al_2O_3, $FAPbBr_xI_{3-x}$ and gold contacts, respectively, were tested at Agilent machine for transfer and output thin-film transistor analysis. ITO and silicon served as gate bottom-contacts and the upper-contacts were both made of gold, drain and source contacts. Four groups of perovskite samples with different bromine contents were analyzed, each group with a total of 5 chemically similar substrates. Present transfer and output analyses were made for transistors with 90µm length and 1400µm width (fig.A1.8 on *Supporting information* appendix).

For transfer curves, devices were swept for a gate voltage range ($-2V \leq V_G \leq 0V$) keeping drain voltage constant ($V_D = -2V$). In output curves, devices were swept for a drain voltage range ($-2V \leq V_D \leq 0V$) with 5 varying gate voltages, ($V_G = 0V, -0.5V, -1V, -1.5V, -2V$). Source voltage V_S was grounded for all transfer and output measurements. High leakage current was only verified for ITO-based $FAPbBr_{0.1}I_{2.9}$ samples (figs. A3.1 and A3.2 on *TFT leakage current* appendix).

Moreover, drain current negative peaks were observed on both transfer and output curves, being related to the ambipolar nature of these films.

3.8.1 Transfer analysis

Concerning overall transfer data, more current negative peaks are observed when ascending bromine contents.

Regarding ITO substrates, higher overall current is achieved by samples with lesser bromine, but these samples also present fewer current downfalls. Bromine addiction tends to create a more symmetrical drain current minimum according to the gate voltage range, meaning a downfall around $V_G = -1V$. These recorded current minimums may be related to ambipolarity, as drain current absolute value ascends for both increasing and decreasing gate voltage. For silicon substrates, overall drain current is much lower than for ITO, current minimums appear in a narrower voltage range, and the overall transfer curve profile is more consistent among these 20 samples. In silicon case, bromine variation doesn't affect the overall current level, as the ratio between highest and lowest displayed currents is 15, whereas for ITO is 10^4 .

Overall drain current is higher for ITO and more negative peaks are visible than for silicon samples, regardless of bromine content. However, overall ITO current diminishes and silicon current slightly destabilizes with increasing bromine content (fig.3.12a, b, c, d).

Regarding literature, ambipolar characteristics were also verified in a very similar perovskite transistor, based on methylammonium iodide ($MAPbI_3$) semiconductor [142].

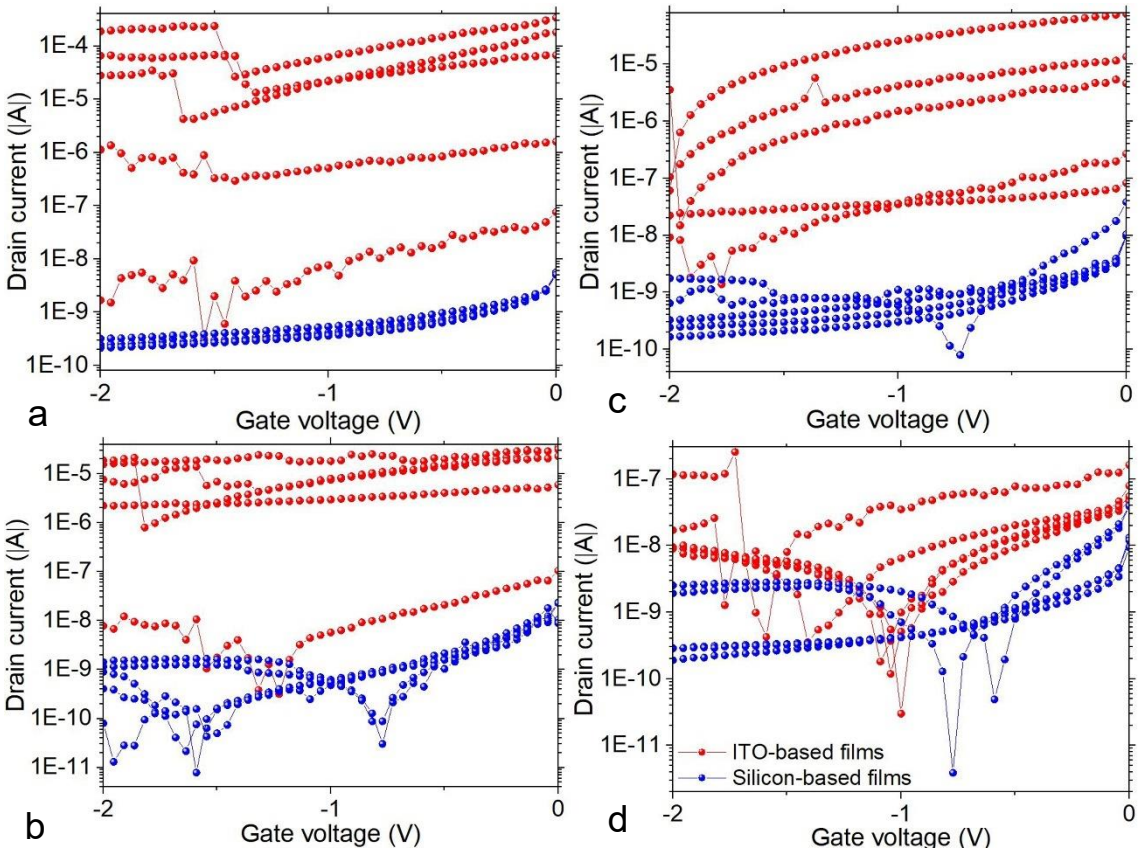

Figure 3.12 – Transfer characteristics of both ITO and silicon-based TFTs. Bromine quantity (x) is 0.1, 0.3, 0.5 and 1 for graphics a), b), c) and d), respectively.

3.8.2 Output analysis

Output data of ITO and silicon TFTs is presented in fig.3.13 and fig.3.14, respectively.

ITO substrates suggest a more consistent output curve profile with higher ambipolar profile than for silicon, according to gate voltage variation. This profile refers to the negative peaks which fall

in the middle of the drain voltage sweep, more specifically around -1V. Plus, a significant shift in output curves takes place when increasing gate voltage negativity, shifting drain voltage downfall peaks closer to $V_D = -2V$. These characteristics are independent of bromine contents. However, there is one exception. For high bromine content ($x = 1$), output curves destabilize, being higher the profile variation for more negative gate voltages as the gradual voltage shift is not consistent for $V_G = -1.5V$, for instance. Also, an increase in bromine to $x = 1$ results in one approximation between all gate voltage negative peaks. (fig.3.13a, b, c, d).

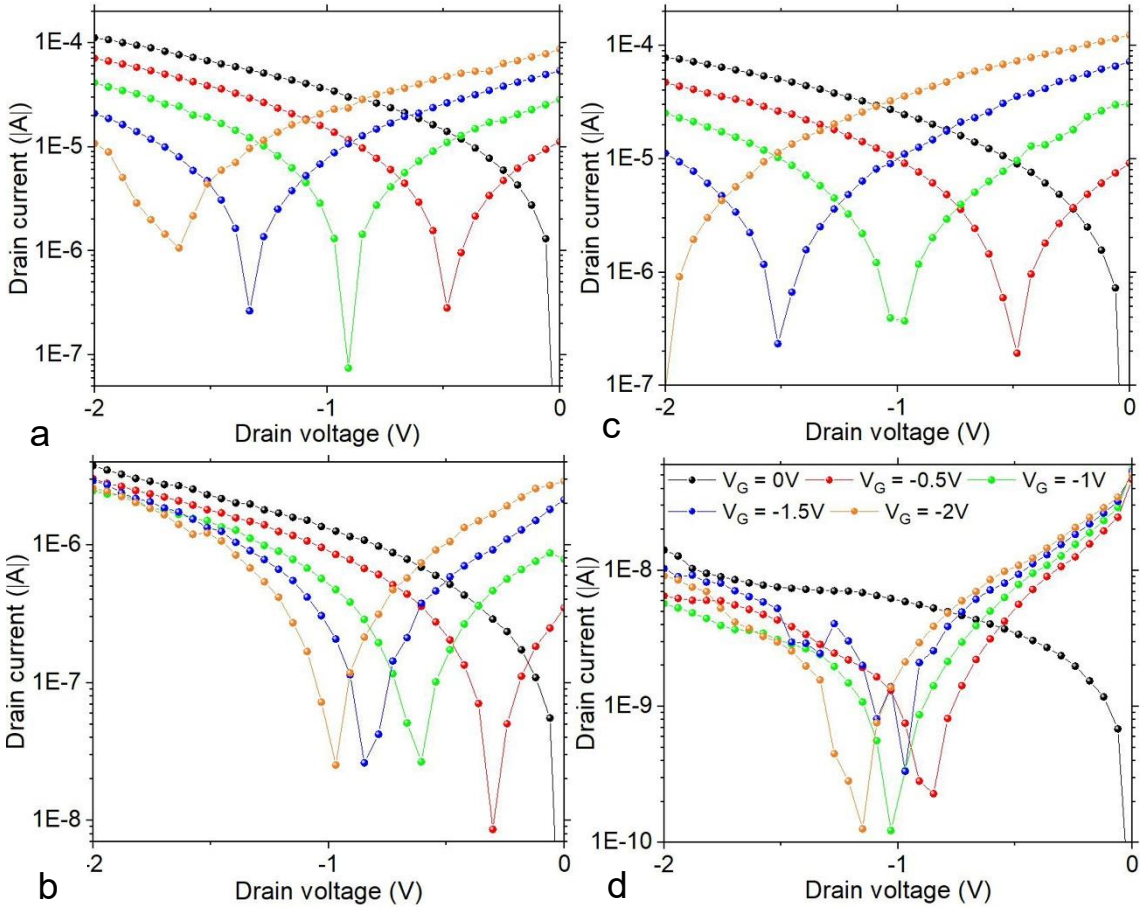

Figure 3.13 – Output characteristics of ITO-based TFTs with both drain and gate voltage sweep -2V to 0V. Bromine quantity (x) is 0.1, 0.3, 0.5 and 1 for graphics a), b), c) and d), respectively.

For silicon TFTs, the same horizontal shift due to gate voltage is not relevant, and all gate voltage curves present their negative peaks around $V_D = -0.5V$, regardless of bromine content. Silicon output curves show more profile variability than those of ITOs, meaning they probably possess less hysteresis capacity. However, silicon TFTs demonstrate ambipolar properties at lower drain voltages, $V_D = 0.5V$ for silicon and $V_D = 1V$ for ITO, considering voltage absolute values (fig.3.14a, b, c, d).

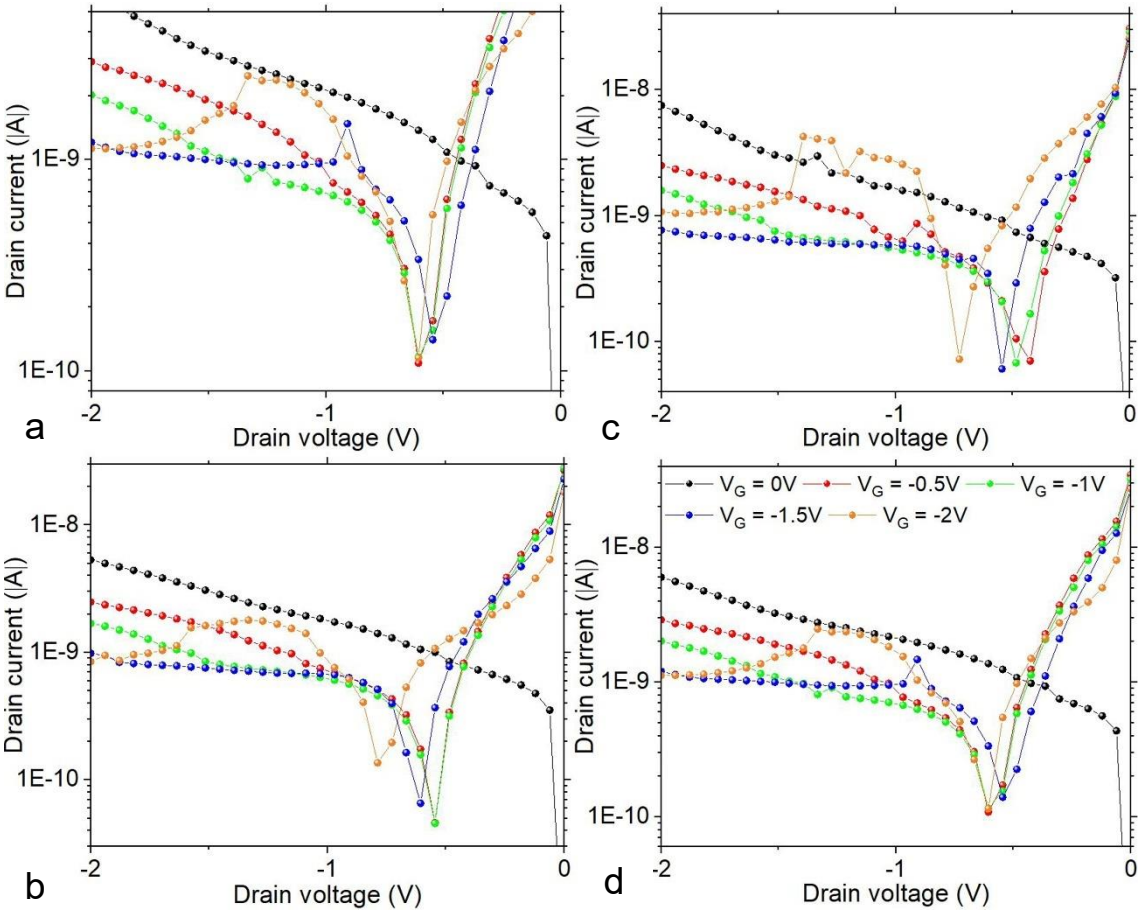

Figure 3.14 – Output characteristics of silicon-based TFTs with both drain and gate voltage sweep -2V to 0V. Bromine quantity (x) is 0.1, 0.3, 0.5 and 1 for graphics a), b), c) and d), respectively.

3.8.3 Field-effect mobility

In order to support Hall carrier mobility data, an estimate for thin-film transistor mobility was developed using field-effect-transistor (FET) method [143]. Since these calculations required capacitance-voltage sweep data, only $FAPbBr_{0.1}I_{2.9}$ and $FAPbBr_{0.5}I_{2.5}$ ITO samples could be subjected to FET method at this time. Field-effect mobility was calculated as a function of the dielectric area ($2.5x10^{-3}$ cm^2), five capacitance-voltage sweeps and current-voltage sweeps, and TFT dimensions (TFT1 with 90µm length and 1400µm width, and TFT2 with 90µm length and 700µm width).

According to results, high and low capacitance variation is observed on both TFT1 and TFT2 devices. FET mobility range of values is smaller for TFT1, showing a more consistent profile than TFT2. The highest mobility value was obtained by one TFT2 simulation, but still not reliable. Regarding $FAPbBr_{0.1}I_{2.9}$ and $FAPbBr_{0.5}I_{2.5}$ devices, its possible to conclude that the capacitance variation of the dielectric is lesser for $FAPbBr_{0.5}I_{2.5}$ TFTs, which probably means aluminium oxide is more stable when incorporating a higher bromine content (fig.3.15).

Overall, estimated mobility during saturation regime achieved by these transistors is similar when compared to literature perovskite field-effect transistors [144-156].
Furthermore, estimated TFT mobilities were also compared to hall-effect mobilities (fig.A1.4 on *Supporting information* appendix).

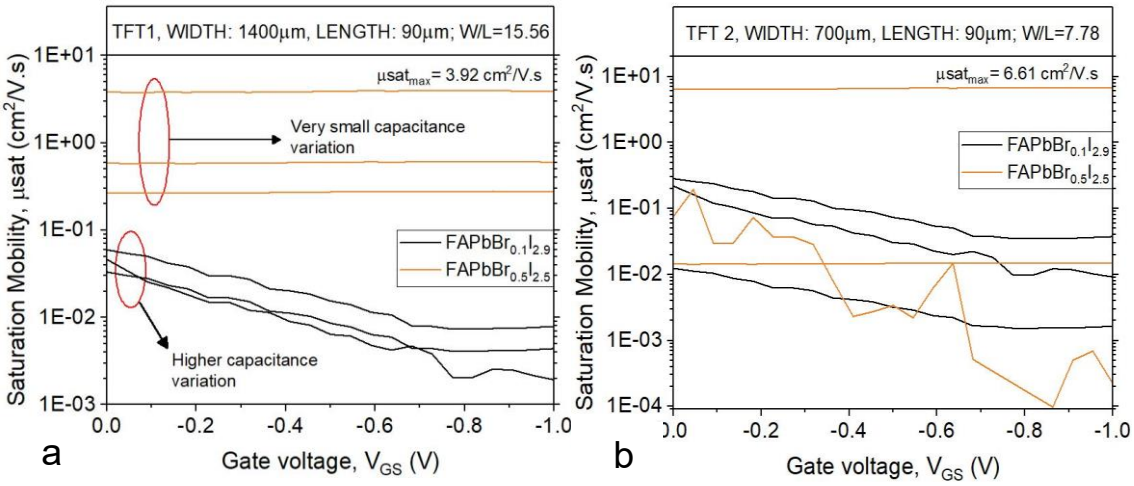

Figure 3.15 – Mobility-voltage sweep using FET method for a) TFTs with 1400µm width, and b) TFTs with 700µm width.

4 Conclusion and future perspectives

Tunable $FAPbBr_xI_{3-x}$ semiconductors could be prepared as solid thin-films. Characterization results show that formamidinium mixed-halide lead-based perovskites reveal potential in several optoelectronic applications, such as ambipolar materials, hall effect high-mobility thin-films, low-energy consumption negative capacitance devices, and fine simulated mobility after TFT application.

According to data, bromine addiction to iodine stabilizes results in all analyzed departments, such as absorbance and thickness, also diminishing device leakage current. Moreover, bromine eliminates most of sample impurities, confers humidity resistance and increases the rate of cubic crystalline structures. Concerning devices performance, increasing bromine content reveals higher p-type charge mobilities and more ambipolar characteristics.

Future perspectives

Lead is an earth-abundant material proving to have exceptional optoelectronic properties, but it's also toxic for humanity and environment, meaning its full replacement in the future would be of great deal for everyone including scientific investigations [157-159]. Lead-free perovskites have already been made, such as bismuth-based or tin-based, presenting a very low or null toxicity level and with promising properties [160-161].
Regardless of lead usage, thin-films with similar properties to the ones in this work reveal potential for semiconducting-based devices, and with a large space for improvement.

For further thin-film transistor research, hysteresis characterization should be done for output and transfer data using both positive and negative sweep, same way was made for metal-semiconductor-oxide capacitors during capacitance-voltage analyses. This TFT analysis can help estimating the amount of grain boundaries inside films and the way they affect polycrystalline devices performance [162].

For the future the addition of more bromine to perovskite solutions is something to be considered. Also, for further investigations, complementary bi-molecular additives such as $PEAI^+$ and SCN^- can be added to solution in order to obtain higher mobilities and disable PbI2 impurity formation [163].

Regarding perovskite thickness, diminishing solution molar concentration and spin-coating rotation would be an advantage when trying to diminish perovskite film thickness [164]. Concerning perovskite deposition, one fabrication challenge still present now-a-days is the production of full cubic-structured film surface under room temperature and humidity. Despite decreasing tolerance factor, a small addition of cesium in the future could be helpful for providing a much higher humidity resistance, disabling hexagonal structure development [165-166].

In the light of this work, plus concerning all sorts of devices based on thin-films, planning several fabrication steps ahead may not be the greatest idea, as many important characteristics appear right after the first fabrication step, which is thin-film deposition. One procedure idea for the future would be to decide the film application only after a very strict thin-film analysis, as properties such as ion migration, negative capacitance and ambipolarity play a very important role on electrical performance and should have the final word on the intended device application.

Bibliography

[1] P. Barquinha, R. Martins, L. Pereira, and E. Fortunato, “Transparent Oxide Electronics: From Materials to Devices. 2012”. [book]

[2] E. Fortunato, P. Barquinha, A. Pimentel, A. Gonçalves, L. Pereira, and R. Martins, “Transparent Electronics-,” vol. 2451, no. V, p. 2829, 2005.

[3] J. F. Wager, D. A. Keszler, and R. E. Presley, Transparent electronics. 2008. [book]

[4] C. I. Bright, Deposition and Performance Challenges of Transparent Conductive Oxides on Plastic Substrates. 2010.

[5] N. S. Foundation, “Major advance made in transparent electronics,” no. December, pp. 1–3, 2004.

[6] J. F. Wager, “APPLIED PHYSICS: Transparent Electronics,” Science (80-.)., vol. 300, no. 5623, pp. 1245–1246, 2003.

[7] J. Gao, K. Kempa, M. Giersig, E. M. Akinoglu, B. Han, and R. Li, “Physics of transparent conductors,” Adv. Phys., vol. 65, no. 6, pp. 553–617, 2016.

[8] R. G. Gordon, “Criteria for Choosing Transparent Conductors,” History, no. August, pp. 52–57, 2000.

[9] R. A. Afre, N. Sharma, M. Sharon, and M. Sharon, “Transparent conducting oxide films for various applications: A review,” Rev. Adv. Mater. Sci., vol. 53, no. 1, pp. 79–89, 2018.

[10] C. I. Bright, “50 Years of Vacuum Coating Technology and the Growth of the Society of Vacuum Coaters”, chapter 7: Review of Transparent Conductive oxides (TCO). 2007. [book]

[11] T. Minami, “New n-Type Transparent Conducting Oxides,” *MRS Bulletin*, vol. 25, no. 8, pp. 38–44, 2000.

[12] T. O. M. T.J. Coutts, J.D. Perkins, and D.S. GinleyMason, “Transparent Conducting Oxides: Status and Opportunities in Basic,” 195th Meet. Electrochem. Soc., no. August, pp. 1–15, 1999.

[13] H. Hosono, “Recent progress in transparent oxide semiconductors: Materials and device application,” Thin Solid Films, vol. 515, no. 15 SPEC. ISS., pp. 6000–6014, 2007.

[14] N. Sarmadian, R. Saniz, B. Partoens, and D. Lamoen, “Easily doped p-type, low hole effective mass, transparent oxides,” Sci. Rep., vol. 6, no. February, pp. 1–9, 2016.

[15] N. Lu et al., “A review of earth abundant ZnO-based materials for thermoelectric and photovoltaic applications,” Oxide-based Mater. Devices IX, vol. 10533, no. February, p. 53, 2018.

[16] G. Hautier, A. Miglio, G. Ceder, G. M. Rignanese, and X. Gonze, “Identification and design principles of low hole effective mass p-type transparent conducting oxides,” Nat. Commun., vol. 4, pp. 1–14, 2013.

[17] J. Xu, J.-B. Liu, J. Wang, B.-X. Liu, and B. Huang, “Prediction of Novel p -Type Transparent Conductors in Layered Double Perovskites: A First-Principles Study,” Adv. Funct. Mater., vol. 28, no. 26, p. 1800332, 2018.

[18] Y. Chen, L. Zhang, Y. Zhang, H. Gao, and H. Yan, “Large-area perovskite solar cells – a review of recent progress and issues,” RSC Adv., vol. 8, no. 19, pp. 10489–10508, 2018.

[19] Z. Yi, N. H. Ladi, X. Shai, H. Li, Y. Shen, and M. Wang, “Will organic–inorganic hybrid halide lead perovskites be eliminated from optoelectronic applications?” Nanoscale Adv., vol. 1, no. 4, pp. 1276–1289, 2019.

[20] Q. Chen et al., “Under the spotlight: The organic-inorganic hybrid halide perovskite for optoelectronic applications,” Nano Today, vol. 10, no. 3, pp. 355–396, 2015.

[21] M. H. Park, J. S. Kim, J. M. Heo, S. Ahn, S. H. Jeong, and T. W. Lee, “Boosting Efficiency in Polycrystalline Metal Halide Perovskite Light-Emitting Diodes,” ACS Energy Lett., vol. 4, no. 5, pp. 1134–1149, 2019.

[22] U. D. M. Von Metallhalogenid-, “Investigation on the material stability of metal-halide perovskite semiconductors.”

[23] J. Chen, S. Zhou, S. Jin, H. Li, and T. Zhai, “Crystal organometal halide perovskites with promising optoelectronic applications,” J. Mater. Chem. C, vol. 4, no. 1, pp. 11–27, 2015.

[24] A. M. Askar et al., “Composition-Tunable Formamidinium Lead Mixed Halide Perovskites via Solvent-Free Mechanochemical Synthesis: Decoding the Pb Environments Using Solid-State NMR Spectroscopy,” J. Phys. Chem. Lett., vol. 9, no. 10, pp. 2671–2677, 2018.

[25] Q. Zhang, F. Hao, J. Li, Y. Zhou, Y. Wei, and H. Lin, “Perovskite solar cells: must lead be replaced–and can it be done?,” Sci. Technol. Adv. Mater., vol. 19, no. 1, pp. 425–442, 2018.

[26] L. C. Chen, Z. L. Tseng, and J. K. Huang, “A study of inverted-type perovskite solar cells with various composition ratios of (FAPBI3)1−x(MAPbBr3)x,” Nanomaterials, vol. 6, no. 10, 2016.

[27] M. I. Asghar, J. Zhang, H. Wang, and P. D. Lund, “Device stability of perovskite solar cells – A review,” Renew. Sustain. Energy Rev., vol. 77, no. April, pp. 131–146, 2017.

[28] Y. Li et al., “Formamidinium-Based Lead Halide Perovskites: Structure, Properties, and Fabrication Methodologies,” Small Methods, vol. 2, no. 7, p. 1700387, 2018.

[29] N. Ahn et al., “Trapped charge-driven degradation of perovskite solar cells,” Nat. Commun., vol. 7, pp. 1–49, 2016.

[30] H. Shen et al., “Improved Reproducibility for Perovskite Solar Cells with 1 cm2Active Area by a Modified Two-Step Process,” ACS Appl. Mater. Interfaces, vol. 9, no. 7, pp. 5974–5981, 2017.

[31] W. G. Li, H. S. Rao, B. X. Chen, X. D. Wang, and D. Bin Kuang, “A formamidinium-methylammonium lead iodide perovskite single crystal exhibiting exceptional optoelectronic properties and long-term stability,” J. Mater. Chem. A, vol. 5, no. 36, pp. 19431–19438, 2017.

[32] Y. Li et al., “Formamidinium-Based Lead Halide Perovskites: Structure, Properties, and Fabrication Methodologies,” Small Methods, vol. 2, no. 7, p. 1700387, 2018.

[33] N. Pellet et al., “Mixed-organic-cation perovskite photovoltaics for enhanced solar-light harvesting,” Angew. Chemie - Int. Ed., vol. 53, no. 12, pp. 3151–3157, 2014.

[34] H. X. Dang et al., “Multi-cation Synergy Suppresses Phase Segregation in Mixed-Halide Perovskites,” Joule, vol. 3, no. 7, pp. 1746–1764, 2019.

[35] “Perovskite fever,” Nat. Nanotechnology, vol. 9, no. 2, p. 837, 2014.

[36] B. Kumar, B. K. Kaushik, and Y. S. Negi, “Organic thin film transistors: Structures, models, materials, fabrication, and applications: A review,” Polym. Rev., vol. 54, no. 1, pp. 33–111, 2014.

[37] Y. Liang et al., “Fabrication of organic-inorganic perovskite thin films for planar solar cells via pulsed laser deposition,” APL Mater., vol. 6, no. 1, 2016.

[38] S. M. Liga, “Components-bandgap relationships in hybrid organic-inorganic perovskites,” Univ. Van Amsterdam, no. February, pp. 1–41, 2017.

[39] S. Ahmad and G. V. Prakash, “Two-step fabrication of R-PbI_4(1-y)Br_4y type light emitting inorganic-organic hybrid photonic structures,” Opt. Mater. Express, vol. 4, no. 1, p. 101, 2014.

[40] L. Kong, G. Liu, J. Gong, Q. Hu, and R. D. Schaller, “Supporting information for Simultaneous band gap narrowing and carrier lifetime prolongation of organic-inorganic trihalide perovskites,” pp. 1–67.

[41] F. Zhang et al., “Two-dimensional organic-inorganic hybrid perovskite field-effect transistors with polymers as bottom-gate dielectrics,” J. Mater. Chem. C, vol. 7, no. 14, pp. 4004–4012, 2019.

[42] S. Tombe et al., “Optical and electronic properties of mixed halide (X = I, Cl, Br) methylammonium lead perovskite solar cells,” J. Mater. Chem. C, vol. 5, no. 7, pp. 1714–1723, 2017.

[43] J. Takeda, T. Tayu, S. Saito and S. Kurita, “Exciton-phonon interaction and potential fluctuation effect in PbI2(1-X)Br2(X) mixed crystals,” Journal of the physical society of Japan, vol. 60, no. 11, pp. 3874-3881, 1991.

[44] M. A. Green, A. Ho-Baillie, and H. J. Snaith, “The emergence of perovskite solar cells,” Nat. Photonics, vol. 8, no. 7, pp. 506–514, 2014.

[45] J. Xu, J.-B. Liu, J. Wang, B.-X. Liu, and B. Huang, “Prediction of Novel p -Type Transparent Conductors in Layered Double Perovskites: A First-Principles Study,” Adv. Funct. Mater., vol. 28, no. 26, p. 1800332, 2018.

[46] G. Kieslich, S. Sun, and A. K. Cheetham, “An extended Tolerance Factor approach for organic-inorganic perovskites,” Chem. Sci., vol. 6, no. 6, pp. 3430–3433, 2015.

[47] G. P. Nagabhushana, R. Shivaramaiah, and A. Navrotsky, “Direct calorimetric verification of thermodynamic instability of lead halide hybrid perovskites,” Proc. Natl. Acad. Sci. U. S. A., vol. 113, no. 28, pp. 7717–7721, 2016.

[48] Anon, “Revolution in conveying finds growing favour in SA,” Certif. Eng., vol. 61, no. 6, pp. 22–23, 1988.

[49] A. Chernatynskiy, A. Auguste, B. Steele, J. E. Phillpot, R. W. Grimes, and S. R. Phillpot, “Elastic and thermal properties of hexagonal perovskites,” Comput. Mater. Sci., vol. 122, pp. 139–145, 2016.

[50] C. J. Bartel et al., “New tolerance factor to predict the stability of perovskite oxides and halides,” Sci. Adv., vol. 5, no. 2, pp. 1–10, 2019.

[51] N. Lu, W. Jiang, Q. Wu, D. Geng, L. Li, and M. Liu, “A review for compact model of thin-film transistors (TFTs),” Micromachines, vol. 9, no. 11, 2018.

[52] A. P. P. Correia, P. Barquinha, and J. C. da P. Goes, “A second-order ADC using sputtered IGZO TFTs,” pp. 5–15, 2015.

[53] V. PANAGIOTIS, “Pixel Design for AMOLED Displays,” 2017.

[54] Z. B. and J. Locklin, “Organic Field effect transistors 2007,” no. i, p. 2007, 2007.

[55] S. Li and D. Chu, “A review of thin-film transistors/circuits fabrication with 3D selfaligned imprint lithography,” Flex. Print. Electron., vol. 2, no. 1, p. 13002, 2017.

[56] E. Fortunato, P. Barquinha, and R. Martins, “Oxide semiconductor thin-film transistors: A review of recent advances,” Adv. Mater., vol. 24, no. 22, pp. 2945–2986, 2012.

[57] Y. Wu et al., “Organic-inorganic hybrid CH3NH3PbI3 perovskite materials as channels in thin-film field-effect transistors,” RSC Adv., vol. 6, no. 20, pp. 16243–16249, 2016.

[58] M. D. Tyona, “A comprehensive study of spin coating as a thin film deposition technique and spin coating equipment,” Adv. Mater. Res., vol. 2, no. 4, pp. 181–193, 2013.

[59] M. D. Tyona, “A theoritical study on spin coating technique,” Adv. Mater. Res., vol. 2, no. 4, pp. 195–208, 2013.

[60] A. H. Makhlouf and I. Tiginyanu, Nanocoatings and ultra-thin films,” Woodhead publishing limited, 2011.

[61] Z. Yang, S. Zhang, L. Li, and W. Chen, “Research progress on large-area perovskite thin films and solar modules,” J. Mater., vol. 3, no. 4, pp. 231–244, 2017.

[62] G. M. Alonzo-Medina, A. González-González, J. L. Sacedón, and A. I. Oliva, “Understanding the thermal annealing process on metallic thin films,” IOP Conf. Ser. Mater. Sci. Eng., vol. 45, no. 1, 2013.

[63] Y. Jiang et al., “The modified multi-step thermal annealing process for highly efficient MAPbI3-based perovskite solar cells,” Sol. Energy, vol. 174, no. August, pp. 218–224, 2018.

[64] G. Dong et al., “Inverted thermal annealing of perovskite films: A method for enhancing photovoltaic device efficiency,” RSC Adv., vol. 6, no. 50, pp. 44034–44040, 2016.

[65] M. R. Ahmadian-Yazdi, F. Zabihi, M. Habibi, and M. Eslamian, “Effects of Process Parameters on the Characteristics of Mixed-Halide Perovskite Solar Cells Fabricated by One-Step and Two-Step Sequential Coating,” Nanoscale Res. Lett., vol. 11, no. 1, 2016.

[66] G. Cotella et al., “One-step deposition by slot-die coating of mixed lead halide perovskite for photovoltaic applications,” Sol. Energy Mater. Sol. Cells, vol. 159, pp. 362–369, 2017.

[67] J. B. Whitaker et al., “Scalable slot-die coating of high performance perovskite solar cells,” Sustain. Energy Fuels, 2018.

[68] P. Fan et al., “High-performance perovskite CH3NH3PbI3thin films for solar cells prepared by single-source physical vapour deposition,” Sci. Rep., vol. 6, no. July, pp. 1–9, 2016.

[69] J. Zhao et al., “Investigation of the hydrolysis of perovskite organometallic halide CH 3 NH 3 PbI 3 in humidity environment,” Sci. Rep., vol. 6, no. March, 2016.

[70] E. Carlos et al., “Boosting Electrical Performance of High-κ Nanomultilayer Dielectrics and Electronic Devices by Combining Solution Combustion Synthesis and UV Irradiation,” ACS Appl. Mater. Interfaces, vol. 9, no. 46, pp. 40428–40437, 2017.

[71] M. E. Cremeens, J. Zimmermann, W. Yu, P. E. Dawson, and F. E. Romesberg, “Supporting Information Supporting Information,” vol. 3, no. 1, pp. 1–5, 1997.

[72] M. M. Rashad, A. M. Elseman, and A. M. Hassan, “Facile synthesis, characterization and structural evolution of nanorods single-crystalline (C 4 H 9 NH 3) 2 PbI 2 X 2 mixed halide organometal perovskite for solar cell application,” Optik (Stuttg)., vol. 127, no. 20, pp. 9775–9787, 2016.

[73] W. Rittisut, J. Padchasri, P. Kidkhunthod, S. Rujirawat, and R. Yimnirun, “Synthesis and characterization of mixed iodide–bromide methylammonium lead perovskite,” Integr. Ferroelectr., vol. 195, no. 1, pp. 19–29, 2019.

[74] D. Barrit et al., “Hybrid perovskite solar cells: In situ investigation of solution-processed PbI 2 reveals metastable precursors and a pathway to producing porous thin films,” J. Mater. Res., vol. 32, no. 10, pp. 1899–1907, 2017.

[75] K. I. Hassoon, M. S. Mohammed, and G. D. Salman, “Characterization of PbI2 thin films prepared by fast vacuum thermal evaporation,” vol. 14, no. 2, pp. 401–406, 2019.

[76] A. A. Petrov et al., “Crystal Structure of DMF-Intermediate Phases Uncovers the Link between CH 3 NH 3 PbI 3 Morphology and Precursor Stoichiometry,” J. Phys. Chem. C, vol. 121, no. 38, pp. 20739–20743, 2017.

[77] B. Slimi, M. Mollar, I. Ben Assaker, A. Kriaa, R. Chtourou, and B. Marí, “Synthesis and characterization of perovskite FAPbBr3−xIx thin films for solar cells,” Monatshefte fur Chemie, vol. 148, no. 5, pp. 835–844, 2017.

[78] K. T. Cho et al., “Highly efficient perovskite solar cells with a compositionally engineered perovskite/hole transporting material interface,” Energy Environ. Sci., vol. 10, no. 2, pp. 621–627, 2017.

[79] B. D. Viezbicke, S. Patel, B. E. Davis, and D. P. Birnie, “Evaluation of the Tauc method for optical absorption edge determination: ZnO thin films as a model system,” Phys. Status Solidi Basic Res., vol. 252, no. 8, pp. 1700–1710, 2015.

[80] M. Miki-yoshida, “Optical Band Gap Estimation of ZnO Nanorods a E = B ^ E - Eg h,” vol. 19, pp. 33–38, 2016.

[81] A. Escobedo-Morales, I. I. Ruiz-López, M. de L. Ruiz-Peralta, L. Tepech-Carrillo, M. Sánchez-Cantú, and J. E. Moreno-Orea, “Automated method for the determination of the band gap energy of pure and mixed powder samples using diffuse reflectance spectroscopy,” Heliyon, vol. 5, no. 4, pp. 1–19, 2019.

[82] A. S. Hassanien and A. A. Akl, “Effect of Se addition on optical and electrical properties of chalcogenide CdSSe thin films,” Superlattices Microstruct., vol. 89, no. January 2019, pp. 153–169, 2016.

[83] I. Levchuk et al., “Brightly Luminescent and Color-Tunable Formamidinium Lead Halide Perovskite FAPbX 3 (X = Cl, Br, I) Colloidal Nanocrystals,” Nano Lett., vol. 17, no. 5, pp. 2765–2770, 2017.

[84] H. Fujiwara and R. W. Collins, Spectroscopic Ellipsometry for Photovoltaics - volume 1: Fundamental Principles and Solar Cell Characterization, vol. 212. 2018.

[85] L. K. Ono, E. J. Juarez-Perez, and Y. Qi, “Progress on Perovskite Materials and Solar Cells with Mixed Cations and Halide Anions,” ACS Appl. Mater. Interfaces, vol. 9, no. 36, pp. 30197–30246, 2017.

[86] Y. Zhao, A. M. Nardes, and K. Zhu, “Mesoporous perovskite solar cells: Material composition, charge-carrier dynamics, and device characteristics,” Faraday Discuss., vol. 176, pp. 301–312, 2014.

[87] D. Liu, C. Yang, M. Bates, and R. R. Lunt, “Room Temperature Processing of Inorganic Perovskite Films to Enable Flexible Solar Cells,” iScience, vol. 6, pp. 272–279, 2018.

[88] J. J. van Franeker, K. H. Hendriks, B. J. Bruijnaers, M. W. G. M. Verhoeven, M. M. Wienk, and R. A. J. Janssen, “Monitoring Thermal Annealing of Perovskite Solar Cells with In Situ Photoluminescence,” Adv. Energy Mater., vol. 7, no. 7, pp. 1–9, 2017.

[89] I. E. Castelli, J. M. García-Lastra, K. S. Thygesen, and K. W. Jacobsen, “Bandgap calculations and trends of organometal halide perovskites,” APL Mater., vol. 2, no. 8, 2014.

[90] Y. Li et al., “Formamidinium-Based Lead Halide Perovskites: Structure, Properties, and Fabrication Methodologies,” Small Methods, vol. 2, no. 7, p. 1700387, 2018.

[91] Z. Li, M. Yang, J. S. Park, S. H. Wei, J. J. Berry, and K. Zhu, “Stabilizing Perovskite Structures by Tuning Tolerance Factor: Formation of Formamidinium and Cesium Lead Iodide Solid-State Alloys,” Chem. Mater., vol. 28, no. 1, pp. 284–292, 2016.

[92] E. Klein, R. Lesyuk, and C. Klinke, “Insights into the formation mechanism of two-dimensional lead halide nanostructures,” Nanoscale, vol. 10, no. 9, pp. 4442–4451, 2018.

[93] F. Li et al., “Ambipolar solution-processed hybrid perovskite phototransistors,” Nat. Commun., vol. 6, pp. 1–8, 2015.

[94] Z. Ren et al., “Thermal assisted oxygen annealing for high efficiency planar CH3NH3PbI3 perovskite solar cells,” Sci. Rep., vol. 4, no. November, 2014.

[95] J. Zhao et al., “Single crystalline CH3NH3PbI3 self-grown on FTO/TiO2 substrate for high efficiency perovskite solar cells,” Sci. Bull., vol. 62, no. 17, pp. 1173–1176, 2017.

[96] Y. Jin et al., “Improvement of Swanepoel method for deriving the thickness and the optical properties of chalcogenide thin films,” Opt. Express, vol. 25, no. 1, p. 440, 2017.

[97] E. R. Shaaban, I. S. Yahia, and E. G. El-Metwally, “Validity of swanepoel’s method for calculating the optical constants of thick films,” Acta Phys. Pol. A, vol. 121, no. 3, pp. 628–635, 2012.

[98] M. Gholami, A. Nazari, K. Azarin, S. Yazdanimeher, and B. Sadeghniya, “Determination of the Thickness and Optical Constants of Metal Oxide Thin Films by Different Methods,” vol. 3, no. 5, pp. 597–600, 2013.

[99] Y. Zhou et al., “Distribution of bromine in mixed iodide-bromide organolead perovskites and its impact on photovoltaic performance,” J. Mater. Chem. A, vol. 4, no. 41, pp. 16191–16197, 2016.

[100] T. Zhang et al., “Crystallinity Preservation and Ion Migration Suppression through Dual Ion Exchange Strategy for Stable Mixed Perovskite Solar Cells,” Adv. Energy Mater., vol. 7, no. 15, pp. 1–10, 2017.

[101] S. Ahmad and G. V. Prakash, “Two-step fabrication of R-PbI_4(1-y)Br_4y type light emitting inorganic-organic hybrid photonic structures,” Opt. Mater. Express, vol. 4, no. 1, p. 101, 2014.

[102] F. Chen et al., “Self-Assembled Growth of Ultrastable CH3NH3PbBr3 Perovskite Milliwires for Photodetectors,” ACS Appl. Mater. Interfaces, vol. 10, no. 30, pp. 25763–25769, 2018.

[103] A. A. Petrov et al., “New Insight into the Formation of Hybrid Perovskite Nanowires via Structure Directing Adducts,” Chem. Mater., vol. 29, no. 2, pp. 587–594, 2017.

[104] D. Choi, S. J. Hong, and Y. Son, “Characteristics of indium tin oxide (ITO) nanoparticles recovered by lift-off method from TFT-LCD panel scraps,” Materials (Basel)., vol. 7, no. 12, pp. 7662–7669, 2014.

[105] O. It, “Lattice structure and index of Indium oxide,” no. 206, 2011. [book]

[106] Z. Ghorannevis, E. Akbarnejad, and M. Ghoranneviss, “Structural and morphological properties of ITO thin films grown by magnetron sputtering,” J. Theor. Appl. Phys., vol. 9, no. 4, pp. 285–290, 2015.

[107] T. Huelser, S. M. Schnurre, H. Wiggers, and C. Schulz, “Gas-phase synthesis of highly-specific nanoparticles on the pilot-plant scale,” Nanotechnol. 2010 Adv. Mater. CNTs, Part. Film. Compos. - Tech. Proc. 2010 NSTI Nanotechnol. Conf. Expo, NSTI-Nanotech 2010, vol. 1, no. November 2014, pp. 330–333, 2010.

[108] A. Zolanvari and H. Sadeghi, “Characterization of annealed Ni/Cu multilayers on Si(100),” 5th Int. Conf. MEMS NANO, Smart Syst. ICMENS 2009, vol. 2, no. 4, pp. 99–101, 2010.

[109] M. N. Khan, M. A. M. Khan, A. S. Al Dwayyan, and J. P. Labis, “Comparative study on electronic, emission, spontaneous property of porous silicon in different solvents,” J. Nanomater., vol. 2014, no. November, 2014.

[110] A. D. Mazzoni, M. S. Conconi, and E. F. Aglietti, “Synthesis of Zr-Si-O-N phases by carbonitriding reaction. Characterization of crystalline phases using the Rietveld method,” Mater. Res., vol. 4, no. 2, pp. 107–111, 2001.

[111] C. Kim, J. W. Park, J. Kim, S. J. Hong, and M. J. Lee, “A highly efficient indium tin oxide nanoparticles (ITO-NPs) transparent heater based on solution-process optimized with oxygen vacancy control,” J. Alloys Compd., vol. 726, no. January, pp. 712–719, 2017.

[112] H. Lee et al., “Effect of Annealing Ambient on SnO2 Thin Film Transistors Fabricated via An Ethanol-based Sol-gel Route,” Electronics, vol. 8, no. 9, p. 955, 2019.

[113] S. Pont et al., “Tuning CH3NH3Pb(I1-:XBrx)3 perovskite oxygen stability in thin films and solar cells,” J. Mater. Chem. A, vol. 5, no. 20, pp. 9553–9560, 2017.

[114] V. L. Pool et al., “Thermal engineering of FAPbI3 perovskite material via radiative thermal annealing and in situ XRD,” Nat. Commun., vol. 8, pp. 1–8, 2017.

[115] A. K. Jena, A. Kulkarni, and T. Miyasaka, “Halide Perovskite Photovoltaics: Background, Status, and Future Prospects,” Chem. Rev., vol. 119, no. 5, pp. 3036–3103, 2019.

[116] W. Rehman et al., “Charge-Carrier Dynamics and Mobilities in Formamidinium Lead Mixed-Halide Perovskites,” Adv. Mater., vol. 27, no. 48, pp. 7938–7944, 2015.

[117] L. M. Herz, “Charge-Carrier Mobilities in Metal Halide Perovskites: Fundamental Mechanisms and Limits,” ACS Energy Lett., vol. 2, no. 7, pp. 1539–1548, 2017.

[118] M. C. Gélvez-Rueda, N. Renaud, and F. C. Grozema, “Temperature Dependent Charge Carrier Dynamics in Formamidinium Lead Iodide Perovskite,” J. Phys. Chem. C, vol. 121, no. 42, pp. 23392–23397, 2017.

[119] O. Gunawan et al., “Carrier-Resolved Photo Hall Measurement in World-Record-Quality Perovskite and Kesterite Solar Absorbers,” 2018.

[120] C. C. Stoumpos, C. D. Malliakas, and M. G. Kanatzidis, “Semiconducting tin and lead iodide perovskites with organic cations: Phase transitions, high mobilities, and near-infrared photoluminescent properties,” Inorg. Chem., vol. 52, no. 15, pp. 9019–9038, 2013.

[121] L. Wang et al., “Tunable bandgap in hybrid perovskite CH 3 NH 3 Pb(Br 3-y X y) single crystals and photodetector applications,” AIP Adv., vol. 6, no. 4, 2016.

[122] P. An and S. Thomson, “Measuring Charge Carrier Lifetime in Halide Perovskite Using Time-Resolved Photoluminescence Spectroscopy,” Edinburgh Instruments, vol. 23, 2018.

[123] L. Kong, G. Liu, J. Gong, Q. Hu, and R. D. Schaller, “Supporting information for Simultaneous band gap narrowing and carrier lifetime prolongation of organic-inorganic trihalide perovskites,” pp. 1–67.

[124] A. A. Zhumekenov et al., “Formamidinium Lead Halide Perovskite Crystals with Unprecedented Long Carrier Dynamics and Diffusion Length,” ACS Energy Lett., vol. 1, no. 1, pp. 32–37, 2016.

[125] R. Brenes et al., “Metal Halide Perovskite Polycrystalline Films Exhibiting Properties of Single Crystals,” Joule, vol. 1, no. 1, pp. 155–167, 2017.

[126] C. Vijila et al., “Relation between charge carrier mobility and lifetime in organic photovoltaics,” J. Appl. Phys., vol. 114, no. 18, 2013.

[127] Q. Han et al., “Single Crystal Formamidinium Lead Iodide (FAPbI3): Insight into the Structural, Optical, and Electrical Properties,” Adv. Mater., vol. 28, no. 11, pp. 2253–2258, 2016.

[128] R. B. Penumala, “Characterization of electric charge carrier transport in organic semiconductors by time-of-flight technique,” Physics (College. Park. Md)., 2012.

[129] I. Grill, “Opto-electronic characterization of charge transport in hybrid perovskite thin film systems for photovoltaic applications,” 2018.

[130] H. Kim, “Capacitance-voltage (C-V) characteristics of Cu/n-type InP schottky diodes,” Trans. Electr. Electron. Mater., vol. 17, no. 5, pp. 293–296, 2016.

[131] I. Mora-Seró et al., “Implications of the negative capacitance observed at forward bias in nanocomposite and polycrystalline solar cells,” Nano Lett., vol. 6, no. 4, pp. 640–650, 2006.

[132] F. Ebadi, N. Taghavinia, R. Mohammadpour, A. Hagfeldt, and W. Tress, “Origin of apparent light-enhanced and negative capacitance in perovskite solar cells,” Nat. Commun., vol. 10, no. 1, pp. 1–9, 2019.

[133] Y. Wang et al., “Ionic behavior of organic-inorganic metal halide perovskite based metal-oxide-semiconductor capacitors,” Phys. Chem. Chem. Phys., vol. 19, no. 20, pp. 13002–13009, 2017.

[134] T. Zhang et al., “Crystallinity Preservation and Ion Migration Suppression through Dual Ion Exchange Strategy for Stable Mixed Perovskite Solar Cells,” Adv. Energy Mater., vol. 7, no. 15, pp. 1–10, 2017.

[135] Y. Shao et al., “Grain boundary dominated ion migration in polycrystalline organic-inorganic halide perovskite films,” Energy Environ. Sci., vol. 9, no. 5, pp. 1752–1759, 2016.

[136] F. Fabregat-Santiago et al., “Deleterious Effect of Negative Capacitance on the Performance of Halide Perovskite Solar Cells,” ACS Energy Lett., vol. 2, no. 9, pp. 2007–2013, 2017.

[137] X. Wang et al., “Van der Waals negative capacitance transistors,” Nat. Commun., vol. 10, no. 1, pp. 1–8, 2019.

[138] G. Monrrabal, B. Ramírez-Barat, A. Bautista, F. Velasco, and E. Cano, “Non-destructive electrochemical testing for stainless-steel components with complex geometry using innovative gel electrolytes,” Metals (Basel)., vol. 8, no. 7, 2018.

[139] J. Škarohlíd et al., “Nanocrystalline diamond protects Zr cladding surface against oxygen and hydrogen uptake: Nuclear fuel durability enhancement,” Sci. Rep., vol. 7, no. 1, pp. 1–14, 2017.

[140] D. D. Liang et al., “Effects of W Addition on the Electrochemical Behaviour and Passive Film Properties of Fe-Based Amorphous Alloys in Acetic Acid Solution,” Acta Metall. Sin. (English Lett., vol. 31, no. 10, pp. 1098–1108, 2018.

[141] M. Metikoš-Huković, Z. Grubač, and S. Omanovic, “Change of n-type to p-type conductivity of the semiconductor passive film on N-steel: Enhancement of the pitting corrosion resistance,” J. Serbian Chem. Soc., vol. 78, no. 12, pp. 2053–2067, 2013.

[142] M. Grätzel, “The light and shade of perovskite solar cells,” Nat. Mater., vol. 13, no. 9, pp. 838–842, 2014.

[143] J. Reynaert, V. I. Arkhipov, J. Genoe, G. Borghs, and P. Heremans, “Current-voltage characteristics in organic semiconductor crystals: Space charge vs. contact-limited carrier transport,” Mater. Res. Soc. Symp. Proc., vol. 846, no. January, pp. 141–149, 2005.

[144] J. Chen, S. Zhou, S. Jin, H. Li, and T. Zhai, “Crystal organometal halide perovskites with promising optoelectronic applications,” J. Mater. Chem. C, vol. 4, no. 1, pp. 11–27, 2015.

[145] S. P. Senanayak et al., “Understanding charge transport in lead iodide perovskite thin-film field-effect transistors,” Sci. Adv., vol. 3, no. 1, pp. 1–11, 2017.

[146] J. Kim, J. Kwon, M. Kim, J. Do, D. Lee, and H. Han, “Low-dielectric-constant polyimide aerogel composite films with low water uptake,” Polym. J., vol. 48, no. 7, pp. 829–834, 2016.

[147] W. Yu et al., “Single crystal hybrid perovskite field-effect transistors,” Nat. Commun., vol. 9, no. 1, pp. 1–10, 2018.

[148] M. K. Li et al., “Intrinsic Carrier Transport of Phase-Pure Homologous 2D Organolead Halide Hybrid Perovskite Single Crystals,” Small, vol. 14, no. 52, pp. 1–8, 2018.

[149] K. Agrawal, V. Gupta, R. Srivastava, and S. S. Rajput, “Perovskite Resonant Tunneling FET with Sequential Negative Differential Resistance Peaks,” ACS Appl. Electron. Mater., vol. 1, no. 5, pp. 735–744, 2019.

[150] G. Wang et al., “Wafer-scale growth of large arrays of perovskite microplate crystals for functional electronics and optoelectronics,” Sci. Adv., vol. 1, no. 9, 2015.

[151] D. B. Mitzi, C. D. Dimitrakopoulos, J. Rosner, D. R. Medeiros, Z. Xu, and C. Noyan, “Hybrid field-effect transistor based on a low-temperature melt-processed channel layer,” Adv. Mater., vol. 14, no. 23, pp. 1772–1776, 2002.

[152] L. Zhu et al., “Synthesis of ultrathin two-dimensional organic-inorganic hybrid perovskite nanosheets for polymer field-effect transistors,” J. Mater. Chem. C, vol. 6, no. 15, pp. 3945–3950, 2018.

[153] C. Huo, X. Liu, X. Song, Z. Wang, and H. Zeng, “Field-effect transistors based on van-der-waals-grown and dry-transferred all-inorganic perovskite ultrathin platelets,” J. Phys. Chem. Lett., vol. 8, no. 19, pp. 4785–4792, 2017.

[154] X. Hu et al., “Direct Vapor Growth of Perovskite CsPbBr3 Nanoplate Electroluminescence Devices,” ACS Nano, vol. 11, no. 10, pp. 9869–9876, 2017.

[155] F. Zhang et al., “Two-dimensional organic-inorganic hybrid perovskite field-effect transistors with polymers as bottom-gate dielectrics,” J. Mater. Chem. C, vol. 7, no. 14, pp. 4004–4012, 2019.

[156] Y. Chen, Y. Chu, X. Wu, W. Ou-Yang, and J. Huang, “High-Performance Inorganic Perovskite Quantum Dot–Organic Semiconductor Hybrid Phototransistors,” Adv. Mater., vol. 29, no. 44, pp. 1–8, 2017.

[157] Q. Zhang, F. Hao, J. Li, Y. Zhou, Y. Wei, and H. Lin, “Perovskite solar cells: must lead be replaced–and can it be done?,” Sci. Technol. Adv. Mater., vol. 19, no. 1, pp. 425–442, 2018.

[158] I. Benabdallah, M. Boujnah, A. El Kenz, A. Benyoussef, M. Abatal, and A. Bassam, “Lead-free perovskite based bismuth for solar cells absorbers,” J. Alloys Compd., vol. 773, pp. 796–801, 2019.

[159] R. Wang, J. Wang, S. Tan, Y. Duan, Z. K. Wang, and Y. Yang, “Opportunities and Challenges of Lead-Free Perovskite Optoelectronic Devices,” Trends Chem., vol. 1, no. 4, pp. 368–379, 2019.

[160] Z. Wang, B. Lei, X. Xia, Z. Huang, K. P. Homewood, and Y. Gao, “CH3NH2BiI3Perovskites: A New Route to Efficient Lead-Free Solar Cells,” J. Phys. Chem. C, vol. 122, no. 5, pp. 2589–2595, 2018.

[161] D. Bartesaghi, A. Ray, J. Jiang, R. K. M. Bouwer, S. Tao, and T. J. Savenije, “Partially replacing Pb 2+ by Mn 2+ in hybrid metal halide perovskites: Structural and electronic properties,” APL Mater., vol. 6, no. 12, 2018.

[162] Y. Shao et al., “Grain boundary dominated ion migration in polycrystalline organic-inorganic halide perovskite films,” Energy Environ. Sci., vol. 9, no. 5, pp. 1752–1759, 2016.

[163] D. H. Kim et al., “Bimolecular Additives Improve Wide-Band-Gap Perovskites for Efficient Tandem Solar Cells with CIGS,” Joule, vol. 3, no. 7, pp. 1734–1745, 2019.

[164] E. Köhnen et al., “Highly efficient monolithic perovskite silicon tandem solar cells: analyzing the influence of current mismatch on device performance,” Sustain. Energy Fuels, vol. 3, no. 8, pp. 1995–2005, 2019.

[165] M. Kulbak et al., “Cesium Enhances Long-Term Stability of Lead Bromide Perovskite-Based Solar Cells,” J. Phys. Chem. Lett., vol. 7, no. 1, pp. 167–172, 2016.

[166] W. K. Chong, D. Giovanni, and T.-C. Sum, “Excitonics in 2D Perovskites,” 2018. [book]

A1 Supporting information

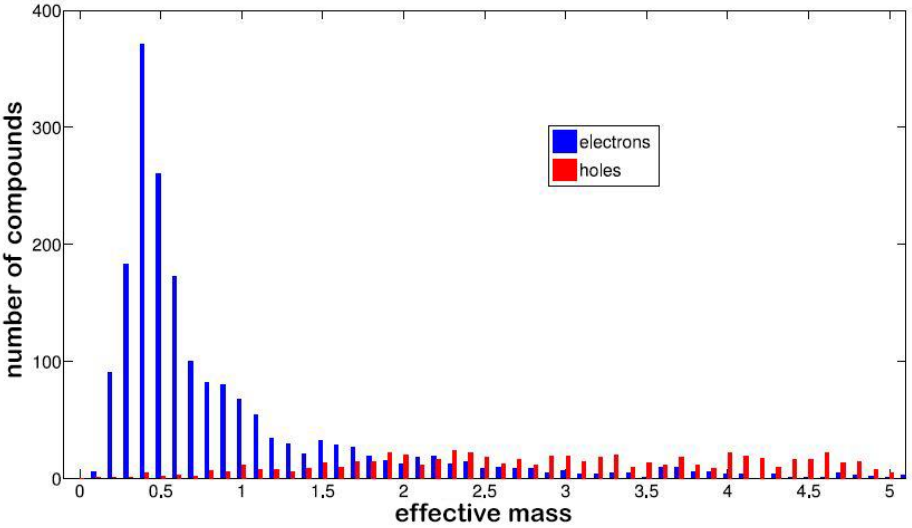

Figure A1.1 – Large hole effective mass (p-type conductors) in comparison to low electron effective mass (n-type conductors) [16].

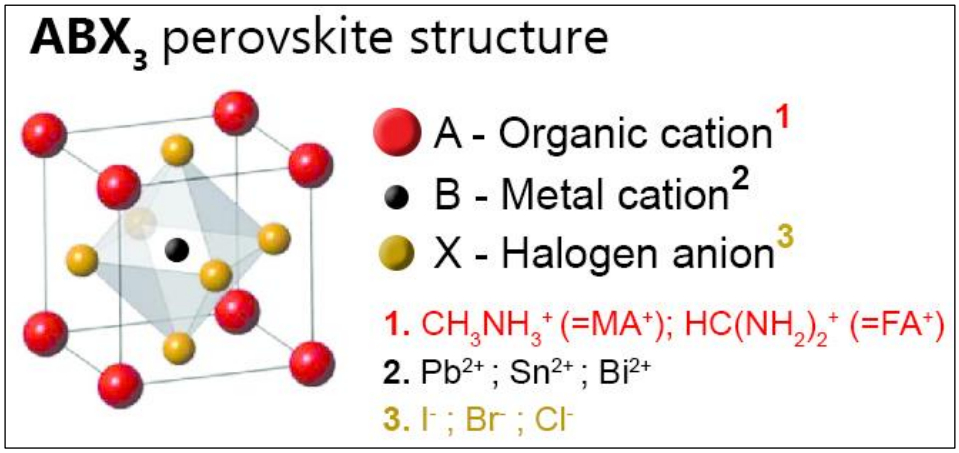

Figure A1.2 – Perovskite structure in higher detail.

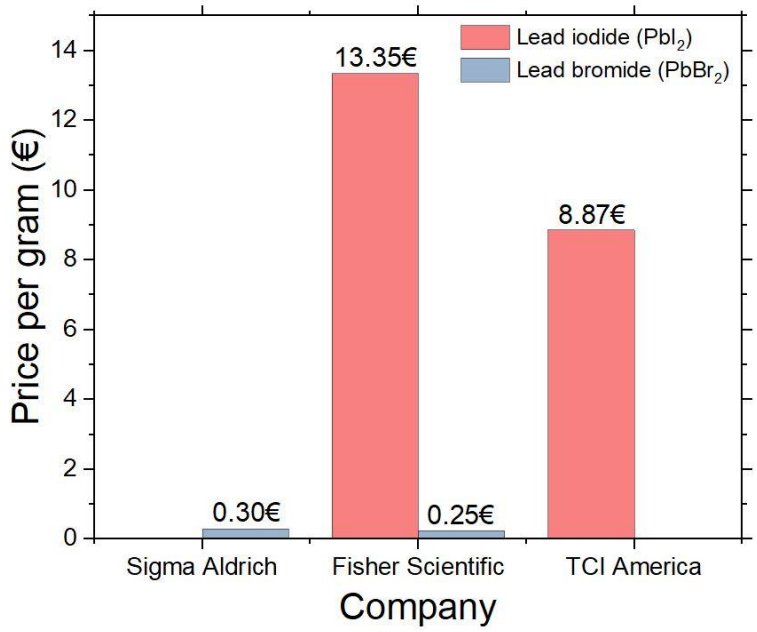

Figure A1.3 – Prices of two reagent powders used for this work, lead iodide and lead bromide, according to distributors Sigma Aldrich, Fisher Scientific and TCI America.

	Mobility units ($cm^2.V^{-1}.s^{-1}$)	
Perovskite device	**$FAPbBr_{0.1}I_{2.9}$**	**$FAPbBr_{0.5}I_{2.5}$**
Metal-semiconductor-metal (MSM) hall mobility (holes)	**4.63**	**18.80 ± 1.40**
MSM hall mobility (electrons)	**15.87 ± 11.24**	**20.2**
TFT 1 saturation mobility (µsat) average range at V_{GS} = -1V	**0.005 ± 0.003**	**2.10 ± 1.82**
TFT 1 highest achieved µsat	**0.06**	**3.92**
TFT 2 µsat average range at V_{GS} = -1V	**0.021 ± 0.019**	
TFT 2 highest achieved µsat	**0.30**	**6.61**

Perovskite device	**$FAPbBr_{0.3}I_{2.7}$**	**$FAPbBr_1I_2$**
Metal-semiconductor-metal (MSM) hall mobility (electrons)	**14.4 ± 0.5**	**38.1**

Low according to literature | Similar to literature | Higher than literature

Figure A1.4 – Obtained carrier mobilities during experimental work.

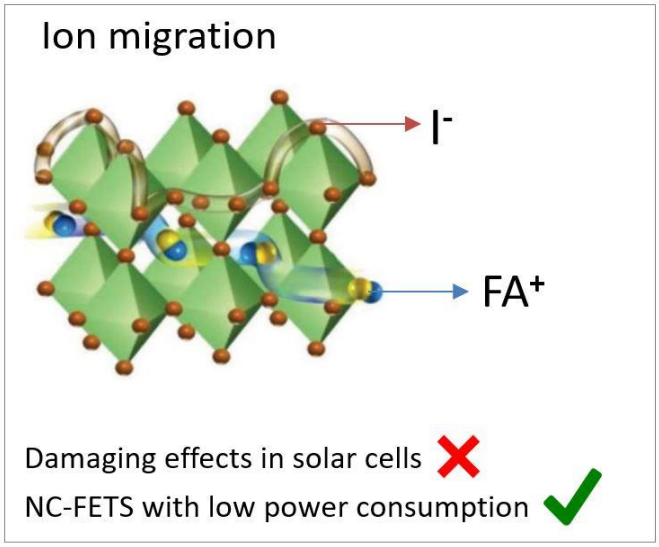

Figure A1.5 – Ion migration behaviour.

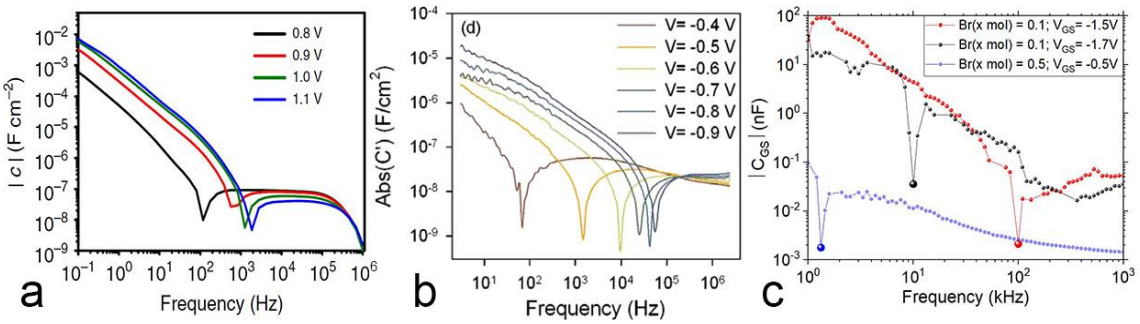

Figure A1.6 – a), b) negative capacitance observed in polycrystalline solar cells [131-132] and c) results obtained during this work.

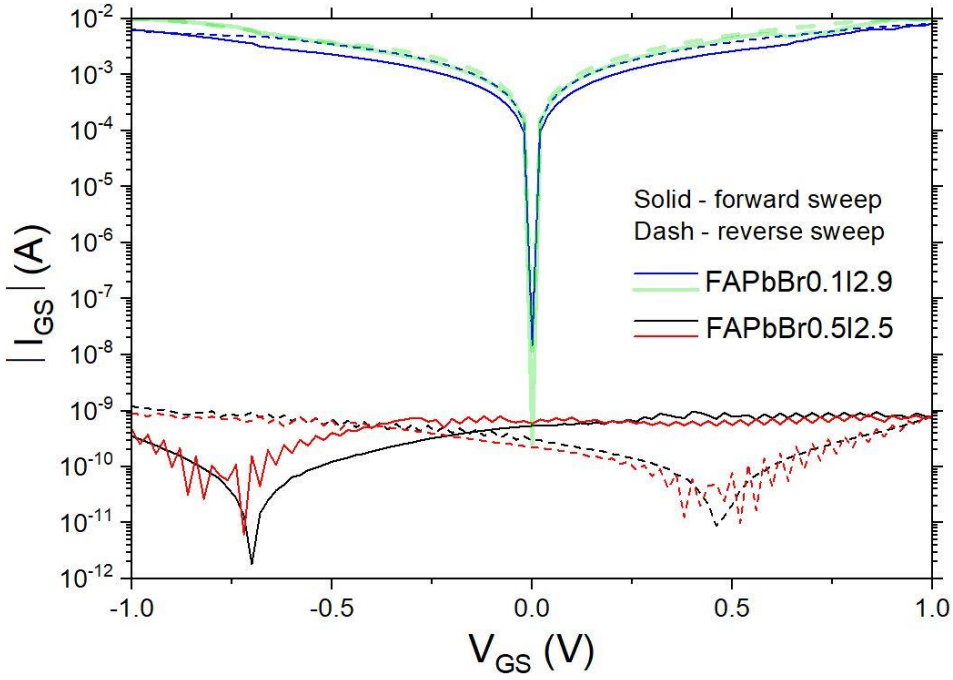

Figure A1.7 – Current-voltage curves for perovskite MOS capacitors containing different bromine content.

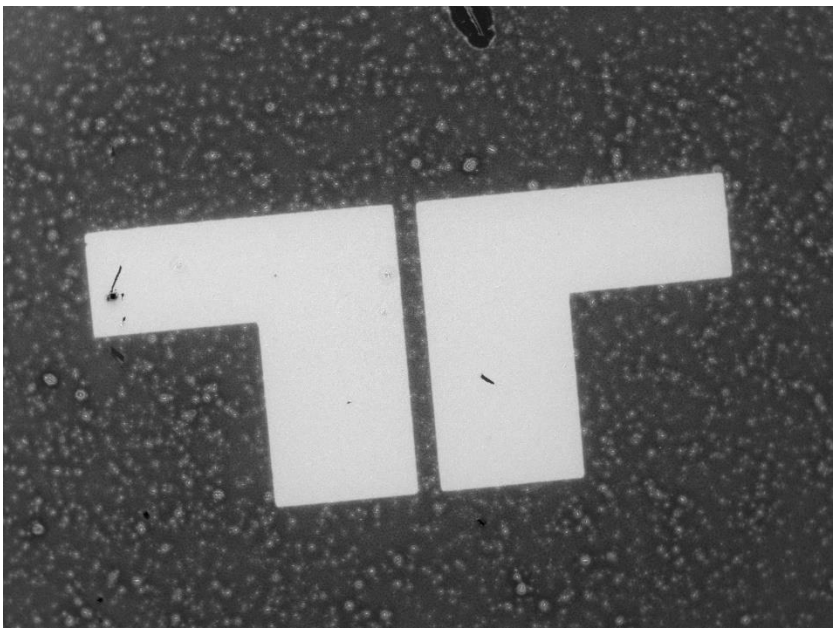

Figure A1.8 – EDX image of 1400um width TFT.

A2 Thin-film images

Figure A2.1 – ITO-coated glass perovskite thin-films with 1M concentration. Upper picture is before thermal annealing, bottom picture is after. On both pictures, the bromine content diminishes from the left to the right. At this concentration, films with more bromine have darker color tones.

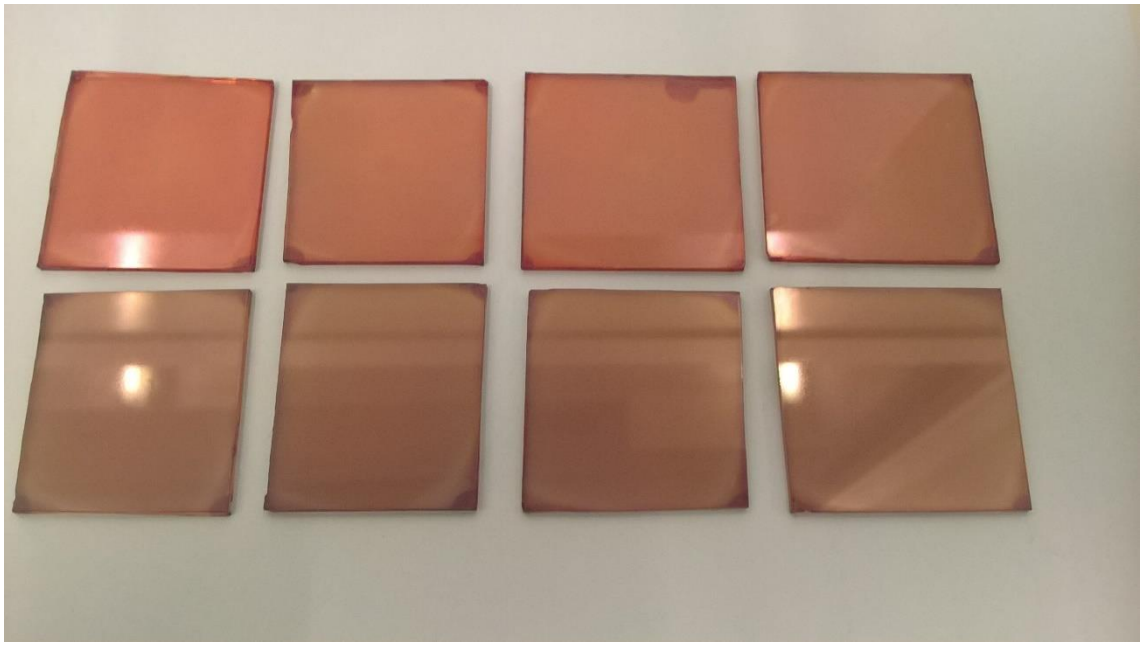

Figure A2.2 – ITO-coated glass FAPbBr2I1 perovskite thin-films with 1M concentration. Upper films were annealed at room temperature, bottom films were thermal annealed at 170º for 30min.

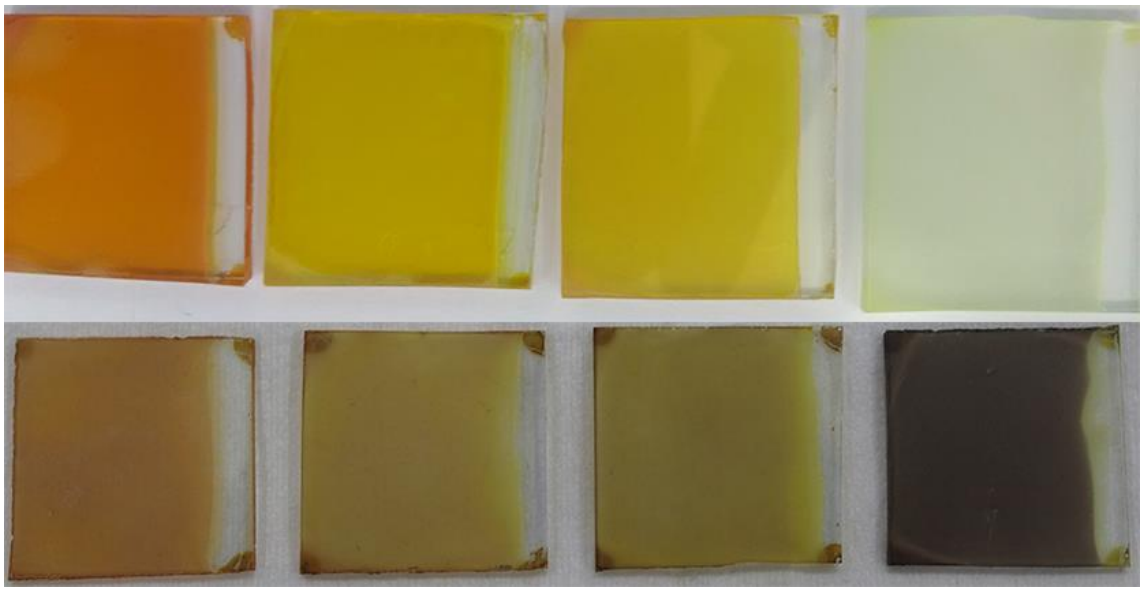

Figure A2.3 - ITO-coated glass perovskite thin-films with 2M concentration. Upper picture is before thermal annealing, bottom picture is after. On both pictures, the bromine content diminishes from the left to the right. At this concentration, films with more iodine have darker color tones.

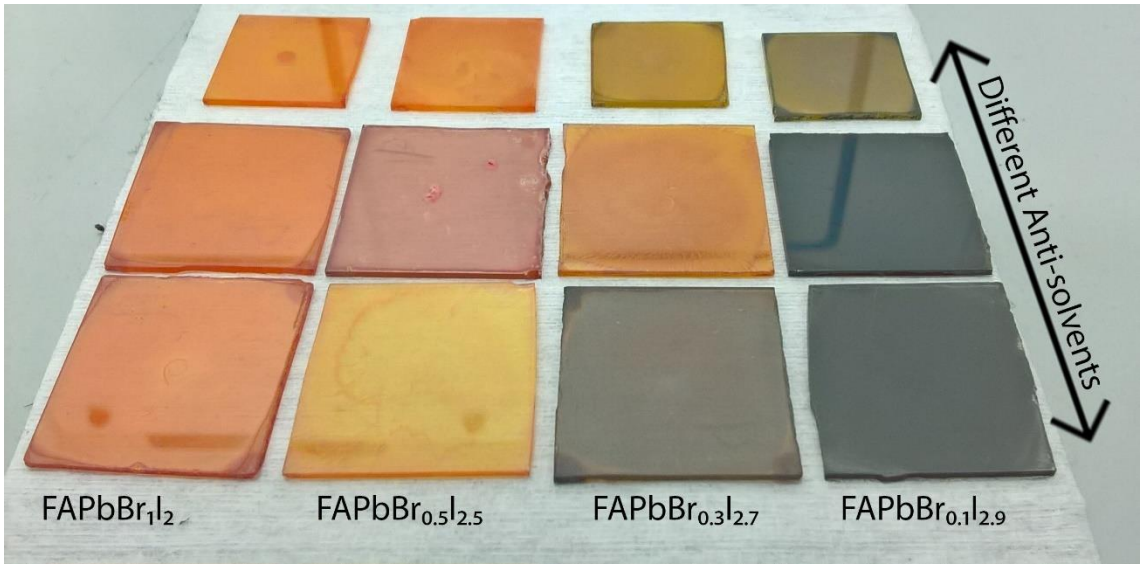

Figure A2.4 – ITO-coated glass thin-films with different anti-solvents for 2M perovskite concentration. Films from middle row were deposited along chlorobenzene anti-solvent, which achieved the highest absorbance (darker tones).

A3 TFT leakage current

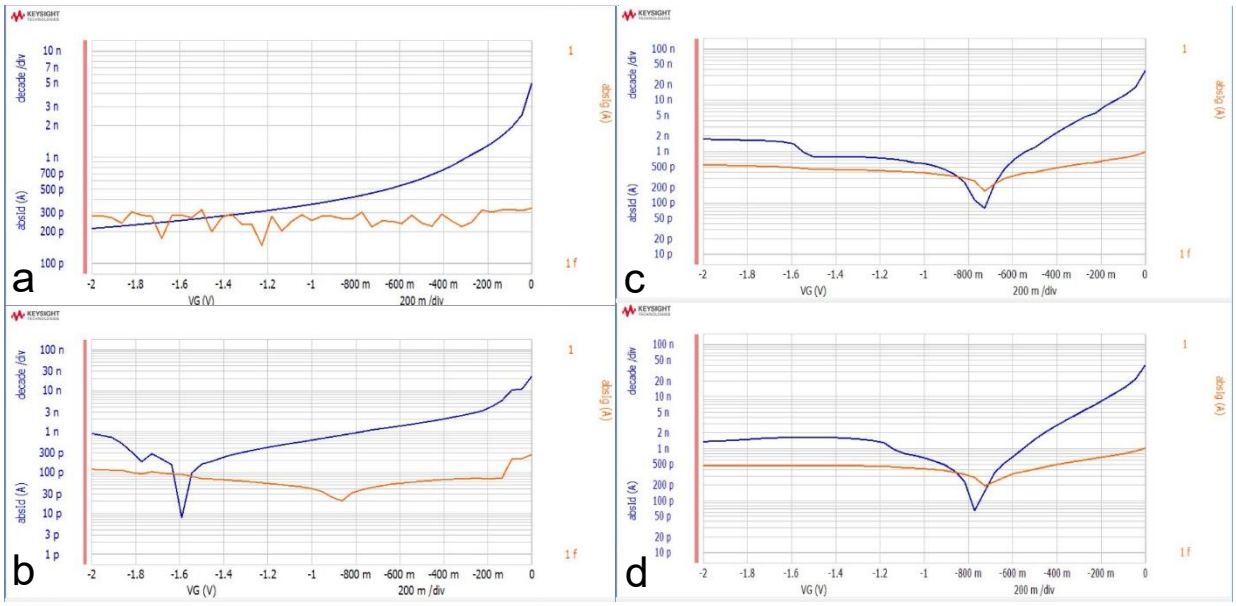

Figure A3.1 – Silicon-based TFTs channel current (blue line) and leakage current (orange line) for bromine molar quantities of 0.1, 0.3, 0.5 and 1, in figures a), b), c) and d) respectively.

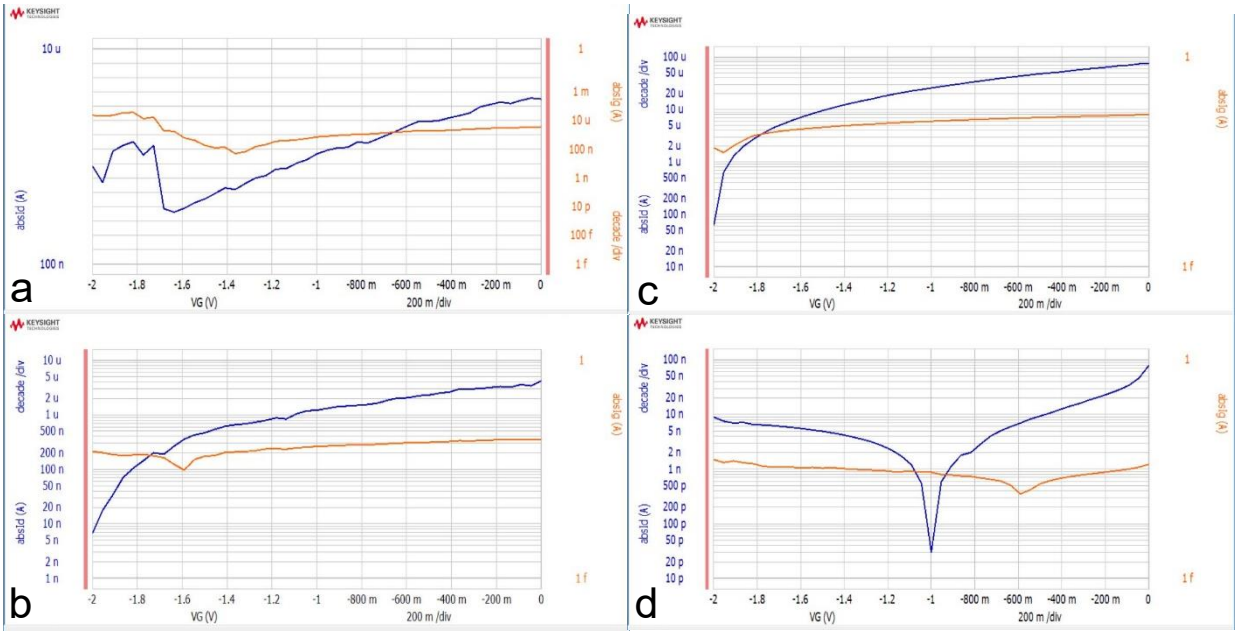

Figure A3.2 – ITO-based TFTs channel current (blue line) and leakage current (orange line) for bromine molar quantities of 0.1, 0.3, 0.5 and 1, in figures a), b), c) and d) respectively.